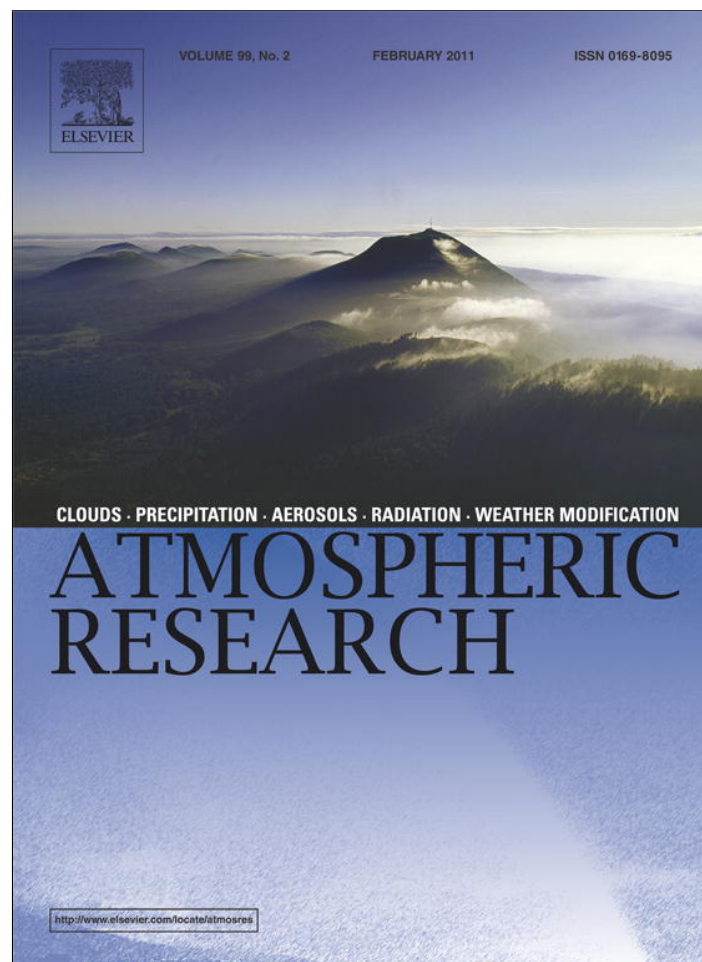


Provided for non-commercial research and education use.
Not for reproduction, distribution or commercial use.



This article appeared in a journal published by Elsevier. The attached copy is furnished to the author for internal non-commercial research and education use, including for instruction at the authors institution and sharing with colleagues.

Other uses, including reproduction and distribution, or selling or licensing copies, or posting to personal, institutional or third party websites are prohibited.

In most cases authors are permitted to post their version of the article (e.g. in Word or Tex form) to their personal website or institutional repository. Authors requiring further information regarding Elsevier's archiving and manuscript policies are encouraged to visit:

<http://www.elsevier.com/copyright>

Contents lists available at [ScienceDirect](http://www.sciencedirect.com)

Atmospheric Research

journal homepage: www.elsevier.com/locate/atmos

Observations of detrainment signatures from non-precipitating orographic cumulus clouds

Yonggang Wang^{*}, Bart Geerts

University of Wyoming, USA

ARTICLE INFO

Article history:

Received 20 April 2010

Received in revised form 7 October 2010

Accepted 22 October 2010

Keywords:

Cumulus detrainment

Orographic cumulus clouds

ABSTRACT

This study uses aircraft in-situ data, airborne mm-wavelength radar data, time lapse photography, and close-proximity radiosonde data to describe the signature of a lifecycle of non-precipitating moist convection left onto the ambient free tropospheric air. The data were collected as part of the 2006 Cumulus Photogrammetric, In-situ and Doppler Observations (CuPIDO-06) campaign, which was centered over the Santa Catalina Mountains, a natural laboratory for the study of the formation and decay of cumulus clouds. This study focuses on one case study, on 8 August 2006, when a series of Cu mediocris formed on the upwind side of the mountain, and decayed on the downwind side. Because these clouds were not precipitating, convective downdrafts were too weak to significantly affect the boundary-layer air downwind of the mountain.

The layer containing orographic cumuli clearly became enriched with moist static energy immediately downwind of the mountain. This enrichment was due to the transport of boundary-layer air by moist convection, and not an artifact of stratified flow over a mountain, since it was mostly caused by an increase in water vapor. Some downwind plumes contained over 50% of the water vapor and moist static energy excess found in orographic cumuli over base values in the upstream environment in the orographic cumulus layer. This enrichment reduces potential instability but increases ambient humidity. This may facilitate successive cumulus growth, although this process of convective conditioning is unlikely to be important for meso-scale (~20 km) orographic convection.

© 2010 Elsevier B.V. All rights reserved.

1. Introduction

Cumulus clouds are important in the general circulation as they dynamically couple the planetary boundary layer to the free troposphere through vertical mass transport and affect the vertical structure of radiative heat flux divergence. The role of Cu convection in the climate system remains a significant challenge as moist convection operates on a range of scales, a significant portion of which is sub-gridscale for climate models. Thus Cu parameterizations have been developed to represent the effect of sub-gridscale convection on the profile of resolved variables, in particular temperature, humidity, and momentum.

Resolved variables change in part in response to detrainment of water and energy from Cu clouds into their cloud-free environment.

Several observational Cu studies have examined the effect of lateral and vertical mixing between cloudy and clear air on the dynamics and microphysics of Cu clouds (e.g., Blyth, 1993; Small and Chuang, 2008). The terminology for the mixing process between cloudy and clear air distinguishes between an entrainment event, which takes place in cloud, and a detrainment event, which evolves outside the cloud edge. Clearly Cu dynamics studies are mostly interested in entrainment, because encapsulation of ambient clear air reduces the cloud's buoyancy by dilution and evaporative cooling. Blyth (1993) describes Cu clouds as shedding thermals, with entrainment occurring near the ascending cloud top and mixed parcels descending around the edges of the thermal

^{*} Corresponding author. Department of Atmospheric Science, University of Wyoming, Laramie, WY 82071, USA.

E-mail address: wyg@uwyo.edu (Y. Wang).

updraft core. This conclusion arose mainly from the analysis of Paluch diagrams (Blyth et al., 1988), which suggests that the source level of much of the diluted air measured at some flight level generally is at a higher level. Damiani et al. (2006) generally confirmed this conclusion using airborne Doppler radar data. These data do not reveal significant penetrative downdrafts, but they illustrate the importance of lateral entrainment at the base of the cloud top vortex ring. A Large Eddy Simulation (LES) study by Heus et al. (2008) however shows that the Lagrangian tracking of air parcels reveals little cloud top entrainment: particle trajectories averaged over the entire Cu cloud ensemble clearly indicate that the main source of entrainment is lateral.

Relatively few observational studies have described the cloud-scale process of Cu decay and detrainment in terms of changes to the environment, although this is what matters for the parameterization of shallow Cu. Some studies have estimated the vertical profile of lateral mass flux across the edge of Cu clouds (e.g., Raga et al., 1990; Barnes et al., 1996), which quantifies the net en-/detrainment rate, but these studies do not characterize the resulting changes in the environment. Perry and Hobbs (1996) use aircraft measurements to show that ambient humidity is significantly enhanced in the clear air on the down- and cross-shear sides of Cu clouds.

The effect of detraining cloudy air on the surrounding clear air has been studied mainly using numerical simulations. Bretherton and Smolarkiewicz (1989) use a two-dimensional (2D) numerical model to study convectively generated subsidence, gravity waves, and turbulent detrainment. They conclude that detrainment is largely governed by the local vertical gradient of buoyancy in cloud: if the buoyancy of a parcel decreases with height, then its lower part is accelerated faster than the upper region, and this induces divergence and detrainment. Taylor and Baker (1991) confirm this conclusion using soundings and aircraft-inferred lateral mass fluxes across the cloud edge, but again they do not depict resulting changes in the environment. Other modeling studies include Carpenter et al. (1998a), who use a 3D cloud model and show that significant detrainment at mid-levels is often caused by collapsing Cu turrets. Many other numerical studies of Cu detrainment exist, all intended to evaluate and improve Cu parameterizations in larger-scale models (e.g., Randall and Huffman, 1982; Cho, 1985; Siebesma and Holtslag, 1996; Luo et al., 2006). Much progress towards an accurate parameterization of shallow Cu has been made recently through the application of LES, e.g. de Rooy and Siebesma (2008). de Rooy and Siebesma (2010) derive LES-validated analytical functions for detrainment in Cu convection. They distinguish between dynamical detrainment, induced by buoyancy-driven vertical accelerations, and smaller-scale turbulent detrainment at the cloud edge.

The present study examines the signature of both dynamical and turbulent detrainment and the decay of convection downwind of a 'hot spot' of Cu growth, a rather isolated mountain. Orographic Cu towers have well-defined regions of growth and decay relative to such mountain. They penetrate well above the boundary layer yet are relatively short-lived, and thus any downstream enrichment of ambient air with boundary-layer air should be rather apparent. The target Cu clouds in this study are relatively shallow (~2 km depth), so

that they do not produce precipitation and convective downdrafts, which would alter the boundary layer. This study does not distinguish between detrainment of cloudy air during the lifespan of a Cu tower, and convective "debris", i.e. evaporating cloudy air at the end of the Cu tower life cycle. The advantage of orographic convection is that its signal can be readily and undeniably attributed to the convection, because the hot spot is geographically fixed and relatively isolated. The description of the Cu's impact on the environment is facilitated not just by the geographic definition, but also by the persistence of the convection, typically for many hours around or shortly after solar noon.

The present study uses aircraft in-situ data, airborne mm-wavelength radar data, fixed-source time lapse photography, and close-proximity radiosonde data to examine how orographic Cu clouds alter the environment within the layer of Cu development. The concept of detecting the effect of Cu on the environment is quite simple. Such detective work is quite simple using high-resolution model output. However the correct detection using observations only is less straightforward and in this regard we believe this study is a first.

This paper is organized as follows: the experimental design and instrument platforms are summarized in Section 2. The results are presented in Section 3, and their implications are discussed in Section 4. Section 5 lists the main conclusions.

2. Data sources

This study uses data collected on 8 August 2006 in the Cumulus Photogrammetric, In-situ and Doppler Observations (CuPIDO-06) campaign (Damiani et al., 2008). Fig. 1 shows the CuPIDO-06 instrument layout around the Santa Catalina Mountains, a relatively isolated mountain range about 30 km in diameter in southeast Arizona, peaking about 2 km above the surrounding plains. On this day a large number of non-precipitating orographic Cu clouds were penetrated by an instrumented aircraft, the University of Wyoming King Air (WKA), which carried a 95 GHz (3.2 mm) Doppler radar, the Wyoming Cloud Radar (WCR), with fixed (non-scanning) antennas pointing up (zenith), down (nadir), and slant-forward (Damiani et al., 2008). The WCR backscatter in shallow, warm, continental Cu clouds (less than ~1 km) may be below the detection threshold of ~-26 dBZ at a range of 1 km, below or above flight level. Droplets tend to be too small to be detected also in the lowest 0.5–1.0 km of non-precipitating CuPIDO-06 Cu clouds without ice, according to independent cloud base estimates (flight tracks near cloud base and radiosonde data). The WCR generally is sensitive enough to detect the warm continental Cu clouds in CuPIDO more than 0.5 km deep. Some Cu clouds on 8 August grew deep enough for ice crystals to form. Being larger than cloud droplets, ice crystals typically produce a stronger WCR echo than cloud droplets, even if their concentration is small.

A series of nine M-GAUS (Mobile GPS Advanced Upper-air Sounding) radiosondes was launched at 30 minute intervals during the 8 August WKA flight, from a location called Windy Point, on the southeast side of the mountain (Fig. 1). The prevailing wind was east-southeasterly on 8 August within the boundary layer and in the Cu layer above, thus the radiosonde data describe the air mass upstream of the mountain. Each radiosonde ascended in clear air at about 5–10 km upstream

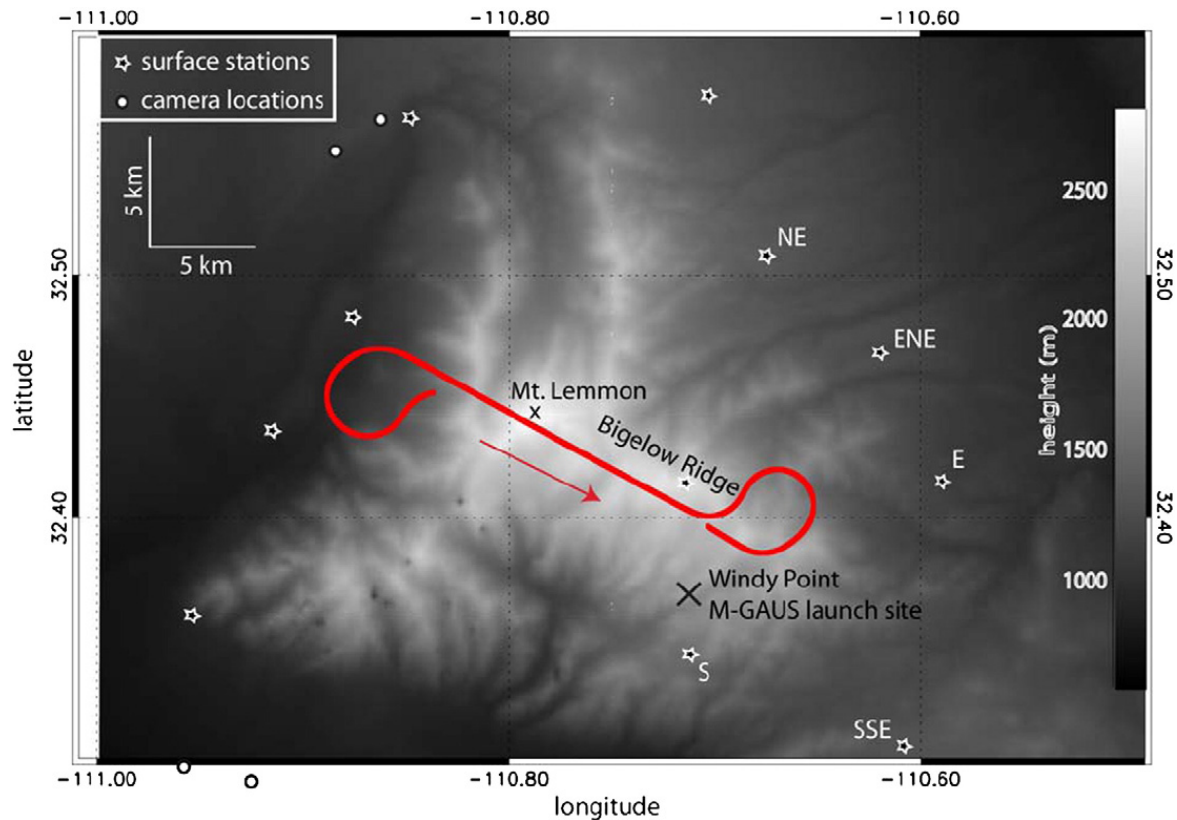


Fig. 1. Terrain map of the Santa Catalina Mountains in southeastern Arizona, showing CuPIDO-06 measurement sites. The city of Tucson stretches across the plains in the lower left of the image. Also shown in red color is an example of typical WKA flight track from 1656:20 to 1703:00 UTC on 8 August 2006. The arrow indicates the flight direction.

of the target orographic Cu clouds. We verified that none of the nine radiosondes penetrated clouds at any level. The temperature and relative humidity sensors, contained in a Vaisala HMP35C probe in the radiosonde, have an accuracy of 0.25 K and 1.5%.¹ Pressure is measured with an accuracy of 0.5 hPa. The accuracy of these measurements matters because we will compare aircraft-based estimates of such variables as equivalent potential temperature (θ_e) and water vapor mixing ratio (r_v) with radiosonde estimates at corresponding levels.

Ten integrated surface flux facility (ISFF) stations were positioned in the foothills around the Santa Catalina Mountains during CuPIDO-06 (Fig. 1). These stations recorded meteorological measurements at five minute intervals. Data from the ISFF stations on the east-southeast side of Mt. Lemmon are used to describe the inflow feeding the orographic Cu, and data from the downwind ISFF stations are used to examine the effect of orographic convection on the convective boundary layer (CBL²), e.g. cooling by convective downdrafts and/or cloud shading.

Two pairs of cameras (Fig. 1) enable stereo-photogrammetric analysis (Zehnder et al., 2007). Only the pair on the southwest

side of the mountain is used, because the prevailing flow was roughly normal to the angle between the cameras and the mountain. The time lapse camera animations,³ at a time resolution of 20 s, nicely illustrate the movement and evolution of Cu clouds over the Santa Catalina Mountains. The stereo-photogrammetric data are used here only to track the cloud top height of the deepest Cu cloud. Cloud top heights are also inferred from the WCR up-antenna reflectivity profiles. WCR cloud tops should be lower than the photogrammetric tops, not so much because of limited radar sensitivity, but rather because the WKA rarely flew precisely below the deepest Cu cloud.

Flight-level thermodynamic and cloud variables are calculated, for instance the wet equivalent potential temperature (θ_q),⁴ and the total water mixing ratio (r_{TOT}). These variables require temperature, mixing ratio, pressure, cloud liquid water content (LWC) and ice water content (IWC). The LWC is inferred from the Forward Scattering Spectrometer Probe (FSSP) (Brenguier et al., 1994), by integrating overall droplet size bins (Table 1). The FSSP LWC estimate does not include any droplets larger than 50 μm in diameter, but it generally compares well (within 10% on average) with that from the Gerber particle volume monitor (PVM-100) (Gerber et al., 1994) and the DMT-100 (Droplet Measurement Technologies) hotwire probe (King et al., 1981) for the 8 August flight. The

¹ See <http://www.eol.ucar.edu/isf/facilities/gaus/gaus.html> for details.

² The CBL is defined as the near-surface mixed layer in which turbulence generation by buoyancy flux dominates (Stull, 1988). In theory this can include the layer of cumulus convection. Practically, we define the CBL as the layer in which potential temperature (θ) and water vapor mixing ratio (r_v) are rather uniform in height. We found that in CuPIDO the CBL is best defined as the center of the lowest 100 m deep layer in which θ increases at least 0.5 K over 100 m and r_v decreases by at least 0.3 g kg^{-1} , with no θ decrease or r_v increase in the next 500 m.

³ QuickTime animation files for 8 August or any other day in CuPIDO-06 can be obtained from http://data.eol.ucar.edu/master_list/?project=CuPIDO.

⁴ The definitions and calculations of equivalent and wet equivalent potential temperatures are based on Bolton (1980).

Table 1

WKA in-situ instruments used in this study.

Parameter	Instrument	Estimated accuracy
Temperature	Reverse flow immersion thermometer	0.5 K
Static pressure	Rosemount 1201F2	0.3–1.0 hPa
Dewpoint temperature	Chilled-mirror dewpoint sensor	1 K
Liquid water content	PMS FSSP 100	± 10%
Cloud droplet concentration	PMS FSSP 100	± 10%
3D air velocity	Gust probe	0.1–0.5 m s ⁻¹

IWC is ignored because ice was essentially absent on all flight legs examined herein. The static pressure measurement on the WKA is quite standard. It is accurate within ~0.3 hPa, except in vigorous Cu clouds, where the accuracy deteriorates to ~1.0 hPa.

Flight-level temperature is measured by a reverse flow thermometer, an immersion probe with an accuracy of 0.5 K in clear air. The reverse flow housing was designed to minimize sensor wetting in cloud. The comparison between cloud entrance and cloud exit composite temperature traces shows that some probe wetting does occur, and thus also evaporative cooling following the aircraft's exit from cloud (Wang and Geerts, 2009). In the present study, the temperature has been corrected for this sensor's evaporative cooling bias following Wang and Geerts (2009).

Flight-level humidity is inferred from a chilled-mirror dewpoint sensor, which has an adequate accuracy (1 K) but has a slow response time. To a first order, the response of this instrument to a step-function change is an exponential adjustment, reaching the actual dewpoint after about 30 s, corresponding with flight track distance of 2.5 km, which is larger than most cloud widths. For derived variables dependent on humidity, such as θ_q , we have to assume in-cloud saturation and slowly varying conditions outside cloud, as measured by the chilled-mirror dewpoint sensor. Because of the slow response of this sensor, we cannot depict an accurate fine-scale detrainment signature immediately outside cloud, within 2.5 km from the cloud edge. Thus we focus on the turn-around loop tracks flown on opposite sides of the orographic convection (Fig. 1). By design these leg-end horizontal loops were not started until at least 30 s after exiting a cloud.

M-GAUS temperature and humidity measurements compare well to the WKA reverse flow thermometer and chilled-mirror dewpoint sensor data in clear air. A comparison based on all WKA flights in CuPIDO-06 yields biases and standard deviations of -0.2 ± 0.7 K (temperature) and $+0.3 \pm 0.4$ g kg⁻¹ (mixing ratio) for the differences between WKA and M-GAUS data, for observations at matching levels, in clear air, within 6 km horizontal separation between the aircraft and the radiosonde. The standard deviations probably are close to the natural variability of temperature and humidity. By design almost all radiosondes were released from the upwind side of the Santa Catalina Mountains during CuPIDO-06; some were released from the peak, Mt. Lemmon [see Table 1 in Damiani et al. (2008) for details].

Finally, we use radiosonde wind data and flight-level vertical and horizontal air velocities. The latter are derived from the WKA gust probe using an established procedure (Lenschow et al., 1991).

3. Results

3.1. Case selection

The 8 August 2006 case (intensive observation period #10, Damiani et al., 2008) was chosen for this study for several reasons. Firstly, convection initially was confined to the mountain footprint (Fig. 2) and was not too shallow (resulting in an insignificant detrainment signal) nor too deep, as lightning poses a hazard to the aircraft. Cumulus convection in an otherwise clear sky started about 3.5 h before local solar noon (1929 UTC) over the Santa Catalina Mountains on 8 August (Fig. 3a). Successive Cu towers gradually deepened for the next 4 h. Eventually their tops were high enough for cloud ice to form, resulting in stronger WCR echoes, but never high enough for lightning to occur. Secondly, the air was relatively dry above the CBL, making a detrainment signature more detectable. Thirdly, the wind was fairly weak at all levels of Cu development (<7 m s⁻¹ in all nine soundings), and rather uniform with height, so that convective towers readily formed over the mountain, without being significantly sheared. The M-GAUS soundings reveal an average wind shear of 0.8 ± 0.3 m s⁻¹ km⁻¹ over the depth of the cloud, mostly from the east. Fourthly, numerous flight tracks were flown along the mean wind direction, which was from the east (between 90 and 110°). This allows contrasting the upstream side with the downstream side of the region of surface-driven Cu convection. Because the convection was clearly confined to the mountain footprint (this was more evident from the cockpit than it is in the coarse-resolution satellite imagery of Fig. 2), the upwind and downwind sides are well defined. The aircraft documented the upwind and downwind regions of the Cu clouds well, because of the 180° turns with a rather large radius of curvature.

The WKA flew a series of legs aligned with Bigelow Ridge (Fig. 1) between 1656 and 1925 UTC, i.e. all before local solar noon. Time lapse photography indicates that shallow orographic Cu first developed near Mt. Lemmon at 1603 UTC. The photography shows that successive Cu towers developed at the eastern side of the Santa Catalina Mountains and drifted towards the west with the prevailing wind. Cu clouds generally formed and drifted along the narrow spine of Bigelow Ridge, which happens to be aligned with the prevailing wind. The convective towers were clearly age-ordered from east to west and generally decayed west of Mt. Lemmon. The maximum cloud top height never grew to the soundings' equilibrium level of 13–14 km MSL, inferred from the 1730–1830 UTC M-GAUS profiles. Instead, convection was capped at about 8 km MSL, except for one tower that reached

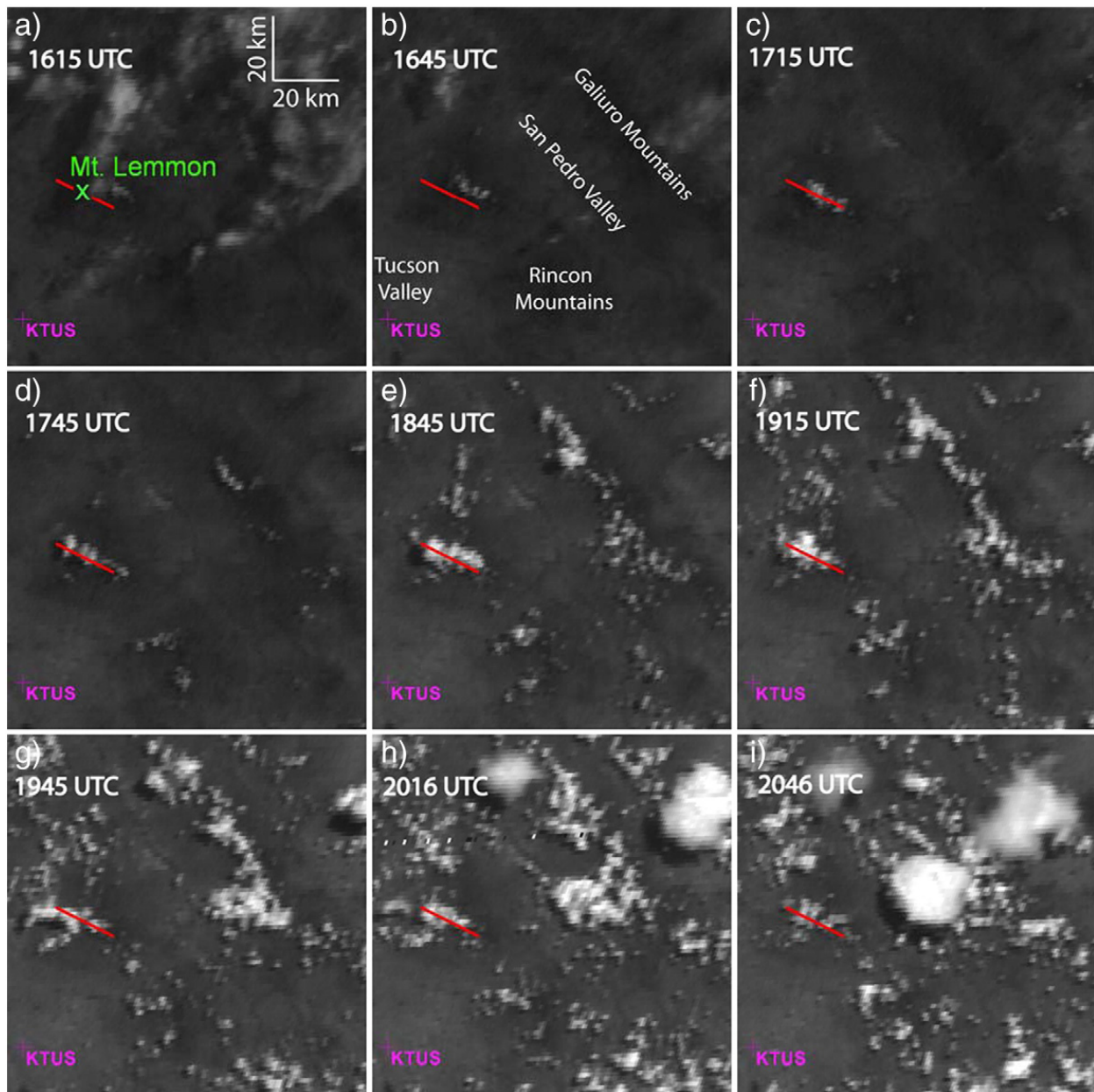


Fig. 2. Series of GOES-11 visible satellite images between 1615 and 2046 UTC on 08/08/2006. The red line indicates the approximate WKA flight track. The outline of the Santa Catalina Mountains and other mountains can be seen as darker regions (lower albedo vegetation), especially around 1715 UTC. Widespread patches of altostratus were present in the morning, and were still visible at 1615 UTC.

a height of 9.1 km at 1950 UTC (Fig. 3a). The WCR-inferred highest cloud top along each flight leg was generally lower than the camera-inferred one, as expected (Fig. 3a). No precipitation shafts were apparent in the time lapse photography during this period.

3.2. Evolution of the boundary layer

We now examine the evolution of temperature and humidity near the surface and in the CBL along the upwind foothills of the mountain, and the resulting change in convective available potential energy (CAPE), in order to understand the observed evolution of Cu tops. It appears that

the first M-GAUS radiosonde (at 1530 UTC, 4 h before local solar noon) was launched before the CBL top reached Windy Point, a rather sharp terrain outcropping about 1.2 km above the Tucson valley (Fig. 4a). The CBL deepened above the elevation of Windy Point shortly after 1530 UTC, and above Mt. Lemmon (about 2.0 km above the valley) during the course of the morning to a maximum height of 3.6 km MSL at 1830 UTC (Fig. 3a). The CBL top probably bulged over the Santa Catalina Mountains (as seen in model output, Demko and Geerts (2010a,b)), i.e. the Windy Point CBL top estimate probably is not representative of a larger area.

Five stations, labeled NE, ENE, E, SSE, and S in Fig. 1, are used to describe the average upwind conditions at the

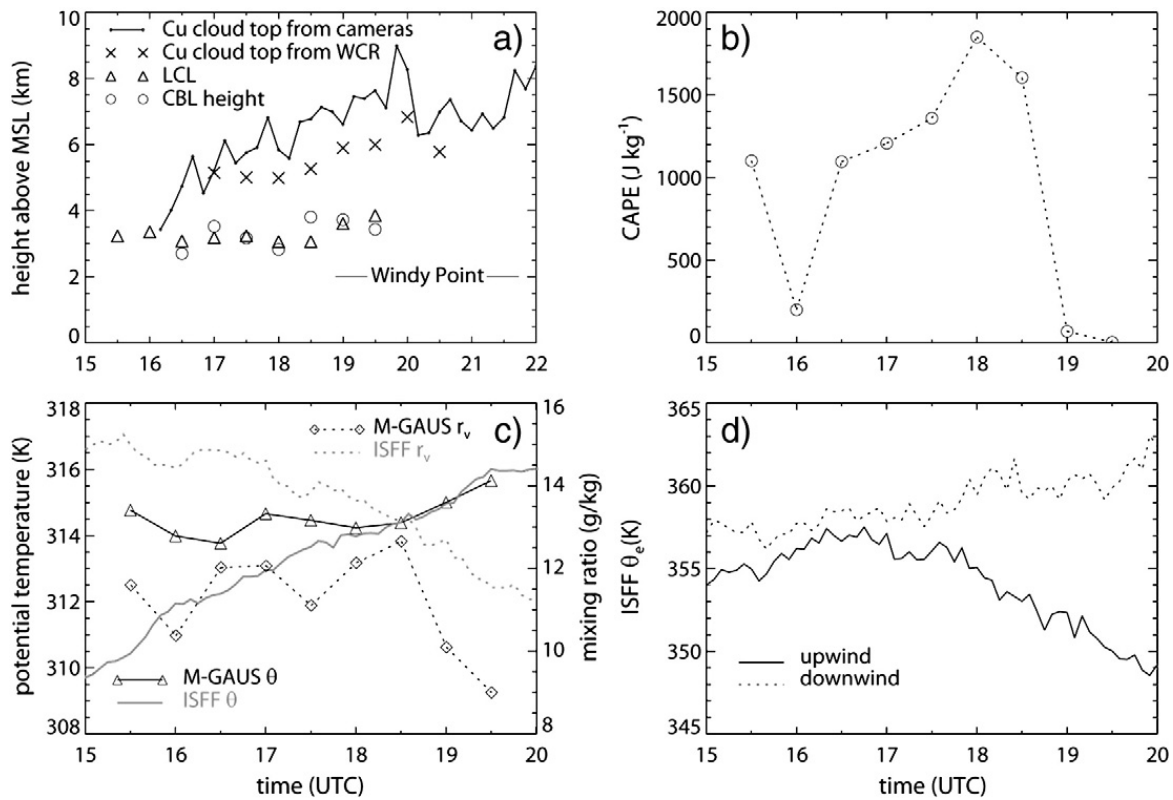


Fig. 3. Evolution of (a) the cloud base (LCL), the CBL height, and highest top of Cu over the Santa Catalina Mountains, (b) mixed-layer CAPE (mixing depth: 50 hPa), (c) CBL and surface (ISFF) potential temperature and mixing ratio and (d) equivalent potential temperature (θ_e) from ISFF stations. The data are inferred from the M-GAUS soundings, ISFF stations, stereo-photogrammetric data, and WCR reflectivity profiles.

surface. The flow at these stations was generally anabatic, with an average anabatic component (defined in Demko et al. (2009)) of 1.8 m s^{-1} during the WKA flight. The average surface θ at the five stations generally increased, and the mixing ratio decreased during the flight (Fig. 3c).

We use the M-GAUS soundings to compute the mean θ and r_v in a layer 100–600 m above Windy Point. These data may better represent the CBL air feeding orographic convection. They confirm an increase in θ , although by only 1–2 K, as opposed to nearly 6 K according to ISFF data for the same period (Fig. 3c), probably because the ISFF measurements are closer to the ground, and the CBL initially was not fully developed in the surrounding foothills. The first three M-GAUS soundings suggest a decrease in CBL θ , but this apparent cooling is because in the first two soundings the CBL top had not reached 600 m above Windy Point level. In fact the 100–600 m AGL layer above Windy Point was 4 K warmer (in terms of θ) than at the surface over the eastern foothills at 1530 UTC (Fig. 3c). This apparent stratification weakened gradually and disappeared by 1800 UTC.

The CBL humidity trend is slightly positive before 1830 UTC, according to the soundings, although drying occurred near the surface, according to the ISFF data (Fig. 3c). Multiple processes can contribute to these trends, mainly advection, turbulent mixing, and surface evaporation. Notwithstanding a substantial latent heat flux, averaging 197 W m^{-2} at the ISFF stations, the observed near-surface drying probably resulted from deeper mixing as the CBL became better established during the morning hours. Both data sources agree on rapid drying between 1830 and 1930 UTC, resulting in an increase in the

lifting condensation level (LCL) (Fig. 3a) and a decrease in CAPE values. The sounding-based mixed-layer CAPE decreased from over 1500 J kg^{-1} at 1830 UTC to under 100 J kg^{-1} half an hour later (Fig. 3b). The upwind surface θ_e started to decrease an hour earlier (Fig. 3d). This lower θ_e may have mixed in the deep CBL and may have been advected over the mountain, reducing the CAPE there. The cloud top height trend lags by over 1 h: a decline in maximum cloud top height started only at 1950 UTC (Fig. 3a). Some of this delay is simply due to the time needed to advect the drier air over Mt. Lemmon, located 12 km downwind of Windy Point.

It is unlikely that the decrease in CAPE after 1800 UTC is a consequence of orographic convection. Convection may cause surface cooling and possibly moistening, by cloud shading and convective downdrafts. Instead a warming and drying trend is observed (Fig. 3c). The CBL above Windy Point is also unlikely to have been affected by the convection, given the persistent easterly flow. Even the downwind ISFF stations appear to have remained unaffected by convection over the Santa Catalina Mountains: θ_e steadily increased there, due to warming, not moistening (Fig. 3d).

It is remarkable that the high CAPE values at 1800–1830 UTC and the lack of convective inhibition ($\text{CIN} < 50 \text{ J kg}^{-1}$; as evident also in the steady growth of Cu convection, Fig. 3a) did not result in deep convection over the mountain. Deep convection did break out around 1945 UTC over the mountain range just (~45 km) east of the Santa Catalina Mountains, resulting in a dense anvil that advected over the Santa Catalina Mountains between 2015 and 2130 UTC (Fig. 2). The resulting shading, and the low-level advection of a patch of dry air,

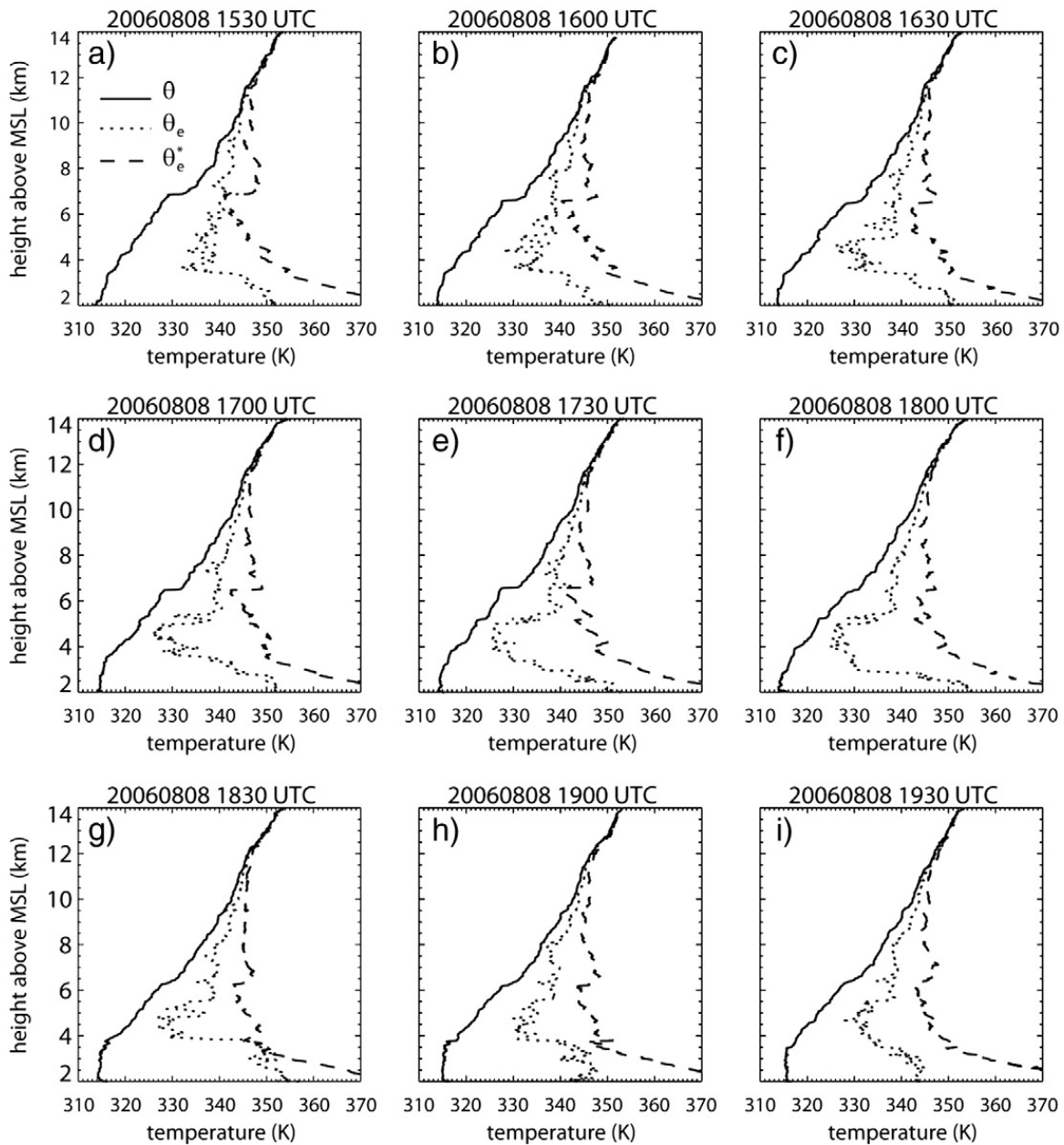


Fig. 4. Profiles of potential temperature (θ), equivalent potential temperature (θ_e), and saturated equivalent potential temperature (θ_e^*) from nine M-GAUS sondes released at Windy Point (Fig. 1).

apparently suppressed deep convection over the Santa Catalina Mountains around 22 UTC at a time when thunderstorms broke out over every other high mountain in the vicinity.

3.3. Evolution of static stability

The M-GAUS soundings are used to examine changes in static stability above the CBL (Fig. 4). θ_e is approximately conserved for a pseudo-adiabatic dry or saturated air parcel and layers in which θ_e decreases with height are potentially unstable (Markowski and Richardson, 2010). θ_e^* corresponds to θ_e for a hypothetically saturated atmosphere; it is not conserved and depends only on temperature. Layers in which θ_e^* decreases with height are conditionally unstable. The spread between θ_e and θ_e^* is a measure of humidity. The vertically

integrated amount of positive difference between θ_e and θ_e^* profiles is a measure of CAPE (e.g., Geerts and Dejene, 2005).

A persistent stable layer just below 7 km MSL (Fig. 5a) apparently capped Cu convection on this day, and locally thwarted deep convection notwithstanding the high CAPE values (Fig. 3b). This stable layer gradually lowered by about 400 m from the first to the last M-GAUS sounding, and it weakened during this period. This weakening is due to warming of the base of the stable layer at ~6.5 km MSL, mainly early in this period (Fig. 5d). The cause of this ~3 K warming, larger than any warming in the CBL, is not detrainment from convection: most of the warming occurred when Cu towers still topped out well below this level (Fig. 3a). Rather the most likely cause is local subsidence, as the mixing ratio decreased in this layer (Fig. 5c). This subsidence could be a gravity wave response to downwind orographic convection at a lower level.

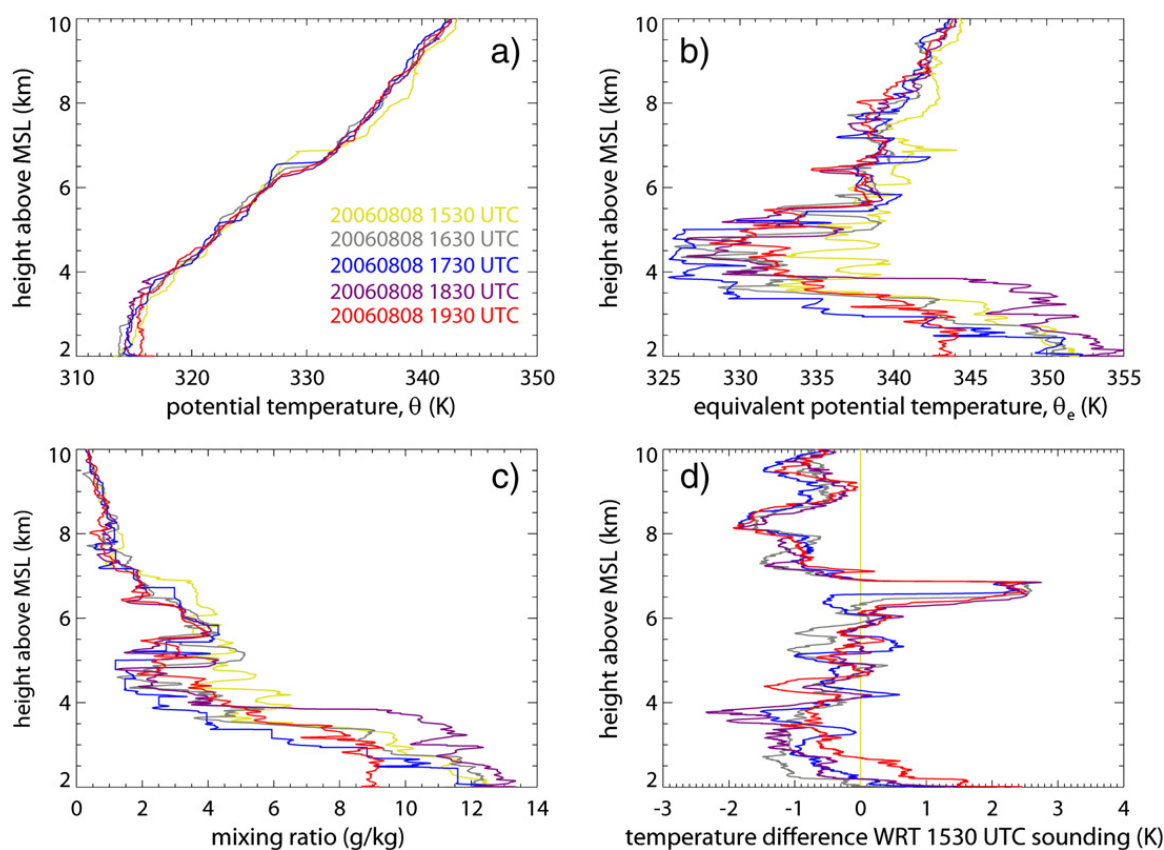


Fig. 5. Changes in thermodynamic profiles between 1530 and 1930 UTC, based on the M-GAUS soundings shown in Fig. 4: (a) θ , (b) θ_e , (c) mixing ratio, (d) temperature difference with respect to the first sounding at 1530 UTC.

A persistent relatively moist layer was present between ~5.2 and 6.6 km, below the stable layer (Fig. 5c). Time lapse photography indicates that a thin layer of altostratus was present in the morning. This layer had mostly evaporated by 1530 UTC (Fig. 2a). The CBL was quite moist (except in the last two soundings), whereas the air above was much drier (Fig. 5c), resulting in strong potential instability, mainly between 2.5 and 4.5 km MSL and between 1700 and 1800 UTC (Fig. 4). This is the layer in which Cu clouds grew over the mountain. The main flight level was at 4.5 km MSL. The large decrease in θ_e between 2.5 km MSL and this flight level (Fig. 5b) increases the probability of detecting a signal of detrainment from rather benign Cu clouds.

3.4. Sequence of radar reflectivity and vertical velocity transects

We now illustrate the structure and evolution of Cu clouds over the Santa Catalina Mountains in a sequence of WCR cross sections collected along straight flight tracks over Bigelow Ridge and further west between 17 and 18 UTC, an optimal time for shallow Cu development according to the stability analysis (Fig. 4). Although the successive flight tracks alternate direction (eastbound and westbound), each transect in Fig. 6 is plotted in the same orientation and is geographically nearly identical, as is evident from the underlying terrain contour. The typical time between transects is 3–6 min, depending on the location along the track: the 90–270° loop maneuvers at each end of a straight flight leg take about 3 min.

The equivalent radar reflectivity generally is quite low, up to -15 dBZ. This is consistent with the lack of particles in the 2D-C and 2D-P probes with diameters of 100 μm or larger. The flight-level temperature was about $+3$ °C for all transects in Fig. 6. The freezing level was about 5.0 km MSL. It is possible that some ice formed in the deeper clouds, but the reflectivity remained below -15 dBZ, and no ice was encountered during later flight legs at 6.5 km MSL, except for a few small ice crystals. Because of the lack of ice crystals or droplets larger than 100 μm , the WCR vertical velocity corresponds well with vertical air motion. The uncertainty of the processed WCR vertical velocity field (Fig. 7) is about 0.3 m s^{-1} (Geerts and Miao, 2005; Damiani and Haimov, 2006).

The Cu clouds are spaced over a distance roughly comparable to their width. Some regions, such as just downwind of Mt. Lemmon (e.g. $-3 < x < -1$ km) have a higher probability to have a cloud overhead than others. Some traceable Cu clouds have been identified with letters (A, B ...) and sometimes numbers (D1, D2 ...) in the radar reflectivity sequence (Fig. 6), and these identifiers have been transferred to the corresponding vertical velocity sequence (Fig. 7). It is remarkable how little continuity transpires in the consecutive WCR transects, mainly in terms of vertical velocity. Of course the apparent rapid change is partly due to the fact that the Cu clouds do not exactly move along the plane of the cross section. The cell movement departed 5–20° from the orientation of the flight tracks, thus some cells moved in or out of these transects. Yet the time lapse camera animations do confirm the rapid evolution of individual Cu towers. The time lapse footage

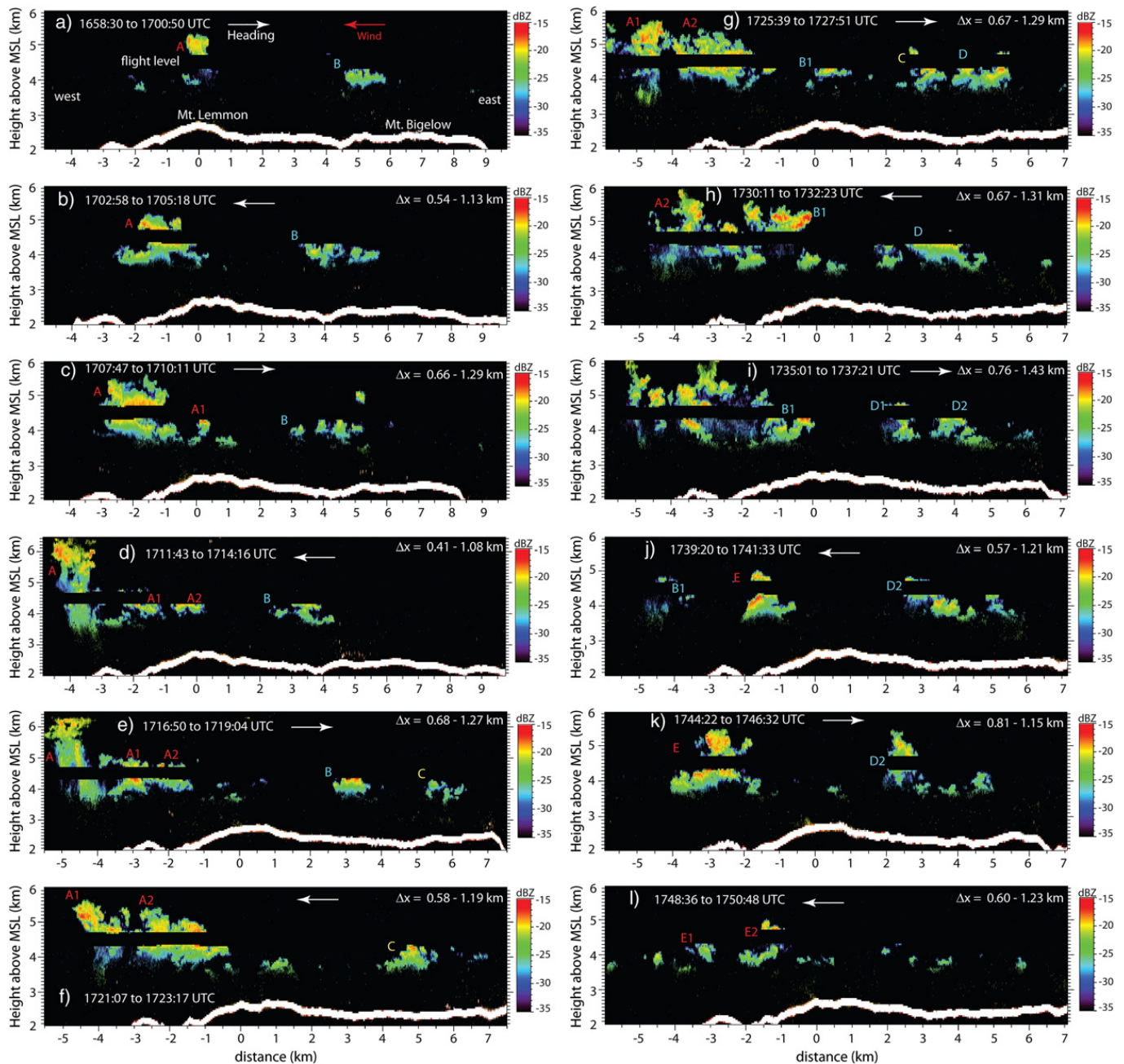


Fig. 6. Sequence of reflectivity transects over the Santa Catalina Mountains, from the WCR nadir and zenith antennas. The flight level is the black belt (radar blind zone). Some of the terrain can be seen at the lower end of the transects. All transects are west (left) to east (right) along a nearly fixed track. The horizontal distance is referenced to the approximate location of Mt. Lemmon. The transect start and end times and the flight direction (white arrow) are shown in each panel. The Δx values shown in the upper right of each panel are the minimum (maximum) westward displacements of tracers between this and the previous section on the uptrack (downtrack) side of this transect, based on the average wind along these transects.

indicates that Cu towers grow rather steadily and collapse suddenly. In some instances, e.g. cloud 'A' in Fig. 6e or 'B1' in Fig. 6j, a cloud had just disappeared from view because the cloud droplets had evaporated, but was still visible on radar because not all larger-size droplets had evaporated.

The 12-panel sequence in Fig. 6, the other transects flow on this day, and the time lapse photography (not shown) indicate that shallow Cu clouds tend to form over Bigelow Ridge (for instance the clouds labeled B, C, D, D1, and D2 in Fig. 6), to be advected westward at a speed corresponding well with the mean wind in Cu layer, about 4.7 m s^{-1} , without experiencing much shear. Some Cu clouds that first formed near Mt. Bigelow

decayed before reaching Mt. Lemmon, e.g. cell 'B' (not captured in a state of collapse) and cell 'D2' (clearly collapsing in Fig. 7k). New Cu clouds tend to form over and just west of Mt. Lemmon, to become the tallest towers over the Santa Catalina Mountains, for instance the clouds labeled A1, A2, B1, and E. It is no surprise that the deepest convection has its roots over the tallest peak in the range. Impressive ascent rates were encountered in some of these towers, for instance tower 'A' had a maximum updraft speed of just over 10 m s^{-1} (Fig. 7b). The Cu clouds all decayed west of Mt. Lemmon. Before vanishing rapidly, these clouds were marked by higher reflectivity values, larger widths, and sometimes rapid subsidence, up to $\sim -10 \text{ m s}^{-1}$ (e.g. cell 'A' in

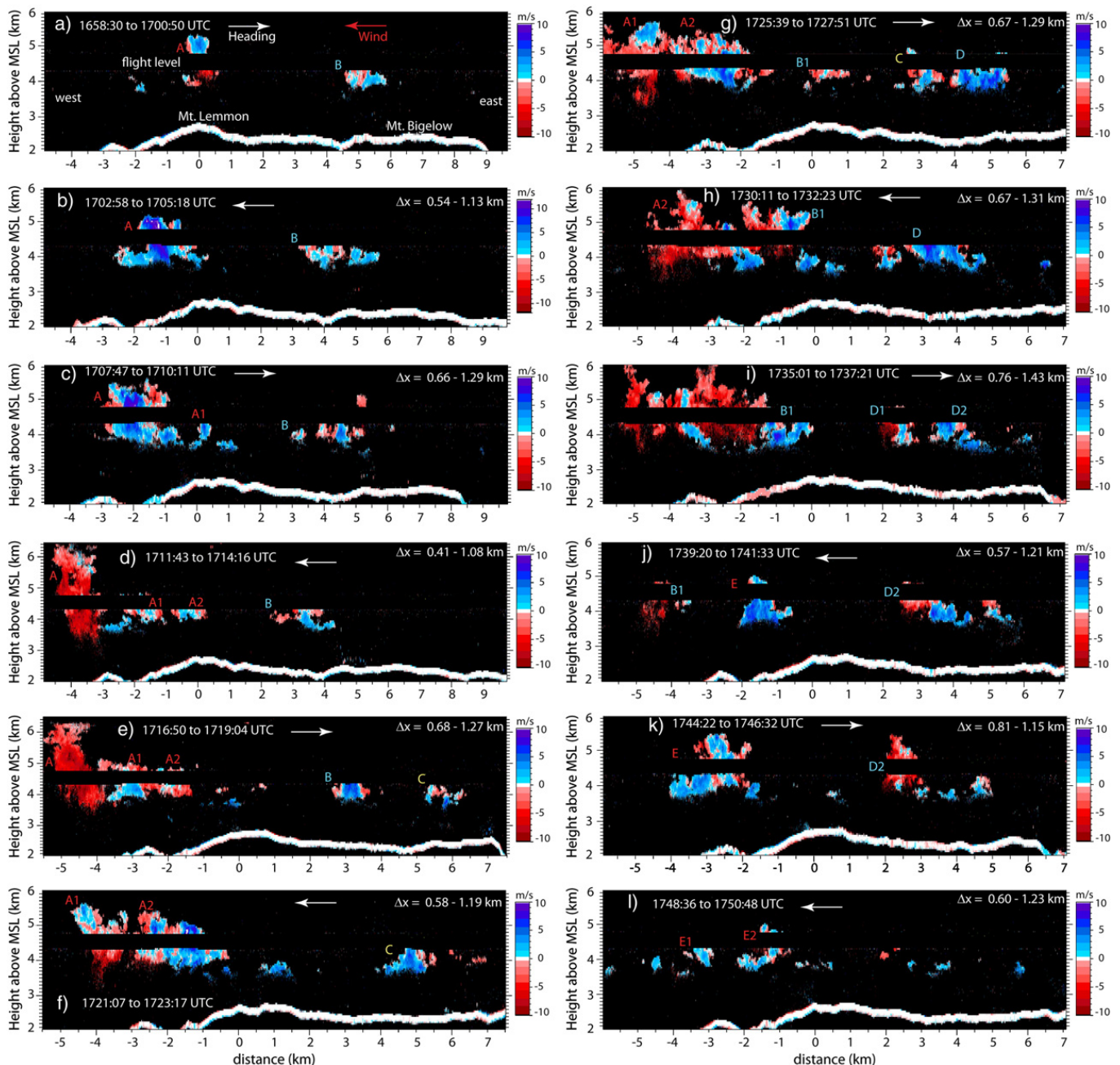


Fig. 7. As Fig. 6, but for WCR vertical velocity.

Fig. 7e). Deeper towers decayed further west because they have a longer lifetime. Decaying towers sometimes retained a small area of ascent near the cloud top (e.g. cell 'A' in Fig. 7d and cell 'A2' in Fig. 7h).

3.5. Flight-level Cu detrainment/decay signatures

We now analyze combined flight-level and remotely sensed WKA measurements and M-GAUS sounding data for eight WKA flight sections, each consisting of a straight leg over the mountain, and two loops, one at each end of the straight leg. Several of the straight legs correspond to particular panels in Fig. 6. The first seven of these eight sections, between 1656 and 1802 UTC, are generally continuous, but they do not include the return straight leg.

The resulting time resolution of this sequence of flight sections is about 9 min. The flight level for this sequence was 4.5 km MSL. The maximum cloud tops remained rather steady at ~5.2 km according to WCR data in the seven transects (Fig. 3a). Outside of the transects, the highest Cu tops were ~1 km higher, according to stereo-photogrammetry. Both the flight level and the peak orographic Cu cloud top were about 1 km higher in the 8th section, flown nearly 1.5 h after the 7th section, at 1920 UTC. At this time the LCL had risen by nearly 1 km (Fig. 3a), because of warming and drying in the CBL (Fig. 3c), thus the cloud depth remained about the same, up to ~2.1 km (~3.2 km) according to 2D WCR (3D photogrammetric) data. Thus the target clouds in all eight sections are relatively shallow (Cu mediocris). Nevertheless, their detrainment signature is quite apparent, as will be shown next.

Each of the eight combined analyses (Fig. 8–Fig. 15) first maps the WKA flight track and the Cu clouds encountered along this track (panel (a)). The flight-level gust probe vertical velocity in each penetrated cloud is shown in panel (a) as well. Next, the upstream environment is contrasted against the downstream environment, in terms of mapped θ_e signatures (panel (a)), a Paluch diagram (panel (b)), and a θ_e profile (panel (c)). The WCR reflectivity transect along the track (panel (d)) indicates cloud vertical structure. The vertical velocity profile of these clouds (panel (e)) qualitatively describes life cycle and level of divergence. And a photo from a forward-looking cockpit camera (panel (f)), shot at the beginning of the flight leg, illustrates the clouds' visual appearance. For the calculation of flight-level θ_e in panels (a–c), it is assumed that the air is saturated in cloud (Section 2). The Paluch diagram in panel (b) is unconventional in that it analyzes not only in-cloud observations, as is common practice (e.g., Paluch, 1979; Carpenter et al., 1998b; Wang and Geerts, 2009), but also flight-level data collected in the clear air either upstream or downstream of the orographic Cu. Both r_{TOT} and θ_q are conserved under pseudo-adiabatic moist processes (Paluch, 1979).

In some sections, such as in Fig. 12 (cloud 'B1'), and Fig. 15 (cloud 'H'), the WCR reflectivity profiles above and below flight level (panel d) suggest that the WKA penetrated a cloud at a location where the FSSP recorded no cloud droplets, i.e. no cloud is shown along the track in panel (a). These clouds were generally subsiding, and as a result most cloud droplets had evaporated. They still contained enough large droplets or ice crystals to be "seen" by the WCR, yet too few for the 2D-C and 2D-P probes to record any. The resolution volume of the WCR is $O(10^4)$ m³, while that of the in-situ 2D particle probes is five orders of magnitude smaller.

In all eight flight sections the mean flight-level wind [shown in panel (a)] is almost aligned with the flight leg orientation (118°), but slightly closer to easterly (ranging between 97 and 112°). The turn-around loops at the end of each straight leg were rather large by design and displaced to the left of the straight legs, so that they nicely cover an area upstream and downstream of the orographic convection. In each of the eight sections, the upwind (eastern) and downwind (western) loops were flown at the same pressure level. Generally θ_e is highest in cloud, and higher in the downwind loop than in the upwind loop. It also tends to be higher just downtrack of clouds, which is an instrument bias (Section 2). The downstream enrichment is highly discontinuous: isolated patches of high θ_e air in the downwind loops, evident in panels (a) of Figs. 8, 9, 12–14, probably result from detrainment from existing Cu clouds, or, more likely, the debris of decayed orographic convection advected downstream.

The Paluch diagrams in panel (b) indicate that the upwind loop is relatively uniform, with θ_q and r_{TOT} values⁵ very close to the M-GAUS values at a corresponding altitude [shown as a black cross on the sounding line in panels (b) and (c)], especially in the earliest sections (Fig. 8–Fig. 11). There are some exceptions, for which we have two possible explanations.

The first one relates to an instrument bias, i.e. the slow response of the chilled-mirror dewpoint sensor (Section 2). The best example for this is the 5th transect (Fig. 12), which shows substantial variability in the upwind loop. In this case the WKA had just exited a Cu cloud near Mt. Bigelow before starting the upwind loop. This cloud can be seen on the far right side in the forward camera image (Fig. 12f).

The second explanation relates to a possible heat reservoir over Mt. Lemmon. As time progressed between 17 and 19 UTC, Cu clouds grew deeper and thus drifted further downwind (west) of Mt. Lemmon. Therefore the straight flight legs were extended further west as well, and as a result the later transects, especially the ones shown in Figs. 14 and 15, had an upwind loop quite close to the highest terrain, sometimes with shallow Cu below flight level. The potential temperature sampled along the upwind loop in Fig. 14 was 1.7 K higher than the M-GAUS potential temperature at this level. The latter is representative of Windy Point further from the mountain peak. This temperature difference is consistent with a warm core over the mountain, resulting in a solenoidal circulation. Both the warm anomaly and the resulting circulation have been observed (Demko et al., 2009) and numerically simulated (Demko and Geerts, 2010a,b), mainly around local solar noon, although they tend to be more shallow, i.e. contained within the CBL. It is possible that the upwind loop in Fig. 14 was at least partly under CBL "dome" over the mountain. Thus the solenoidal forcing may explain the slightly higher θ_e in the upwind loop than above Windy Point (Fig. 14c). Both factors (one an instrument bias and the other a real process) may explain the rather elevated θ_e in the upwind loop of the last flight section (Fig. 15).

The fact that the $[\theta_q, r_{TOT}]$ properties of air in the downwind loop are more distinct from the environment (as measured by the upwind radiosonde) and more similar to cloudy air than air in the upwind loop suggests that the downwind air mass is substantially enriched with cbl air [panels (b) and (c)]. The mean θ_e in the downwind loop corresponds with ambient θ_e values encountered ~0.5–2.0 km below flight level, although it remains much lower than the θ_e values within the cbl [panel (c)]. The downstream enrichment signature is quite clear in this case study precisely because of the significant drop in θ_e from the cbl to flight level.

The differences between "downwind" and "upwind" air properties and between "downwind" and "in-cloud" properties indicate that both unmodified ambient air and former cloud material (detrained from cloud or cloud detritus) are sampled in the downwind loop. The linear alignment of $[\theta_q, r_{TOT}]$ values encountered along the downwind loops of most sections suggests different mixing fractions of these two sources of air [panel (b)]. Downwind air parcels whose $[\theta_q, r_{TOT}]$ values are closer to the corresponding values in cloud than to those found upwind (described by sounding or upwind flight loop) originate mostly within the orographic Cu clouds. Many downwind air parcels have $[\theta_q, r_{TOT}]$ values very close to those found upwind: they are largely unmodified ambient air advected over the mountain in between the Cu towers. Note that the in-cloud $[\theta_q, r_{TOT}]$ values may be slightly overestimated because it is assumed that the cloudy air is saturated, which is not always the case. Relative humidity values under 100% are not uncommon in cloud, especially near the Cu cloud edge (Wang and Geerts, 2010).

⁵ Note that $r_v = r_{TOT}$ outside of cloud.

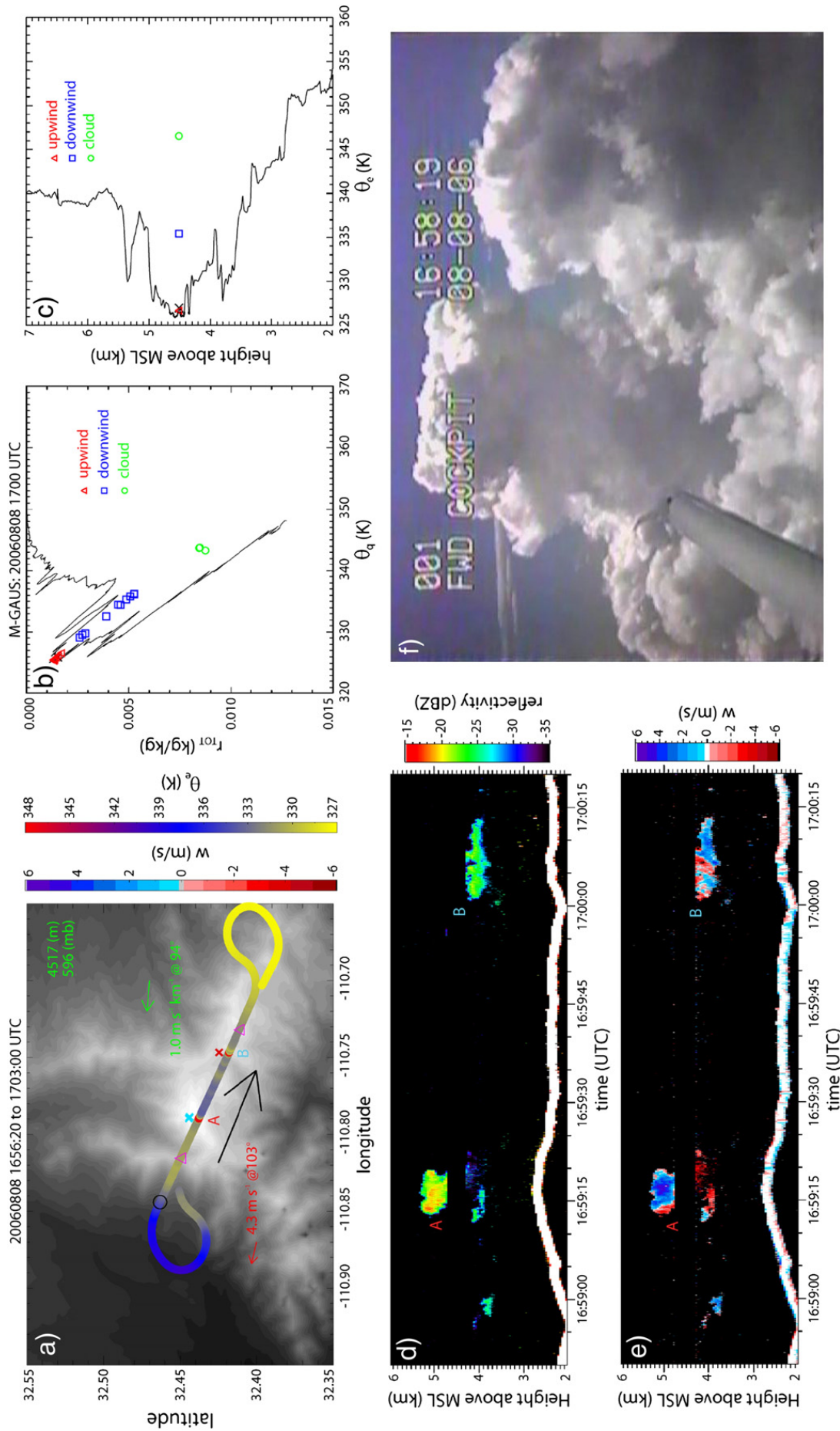


Fig. 8. Cumulus detrainment analysis for the WKA flight track from 1656:20 to 1703:00 UTC on 8 August 2006. (a) Map of the flight track, colored by θ_e over a terrain map (grayscale, with white representing the elevation of Mt. Lemmon, 2791 m). Also shown is the flight-level vertical air velocity (colored crosses, displaced slightly north of the track). The flight level for this track is listed in the upper right corner in green, in MSL height and pressure units. The large black arrow indicates the flight direction. The mean flight-level wind (red vector) and wind shear (green vector) are inferred from the nearest-in-time M-GAUS sounding released at Windy Point, and are computed over the depth of the Cu (cloud base to top). (b) Paluch diagram showing WKA cloud penetrations and out-of-cloud WKA data along the flight turns on the west (downwind) and east (upwind) sides of the orographic convection. Also shown is the nearest M-GAUS sounding. (c) Average θ_e values for the WKA turns on the downwind and upwind sides of the orographic convection, average θ_e value of the cloud penetrations, and M-GAUS θ_e profile. The flight level is indicated with a black cross on the M-GAUS profile in (b) and (c) (in this case the cross is hidden under the red triangles in b). (d) Vertical transect of WCR reflectivity above and below flight level for the straight portion of this track, between the pink triangles shown in (a); the flight level is the black belt (radar blind zone), and the mountain terrain can be seen below. (e) As in (d), but WCR vertical velocity. (f) Cu photo taken by a forward-pointing camera in the cockpit of the WKA at a time shown in the upper right corner of the location shown as a black circle on the flight track in (a).

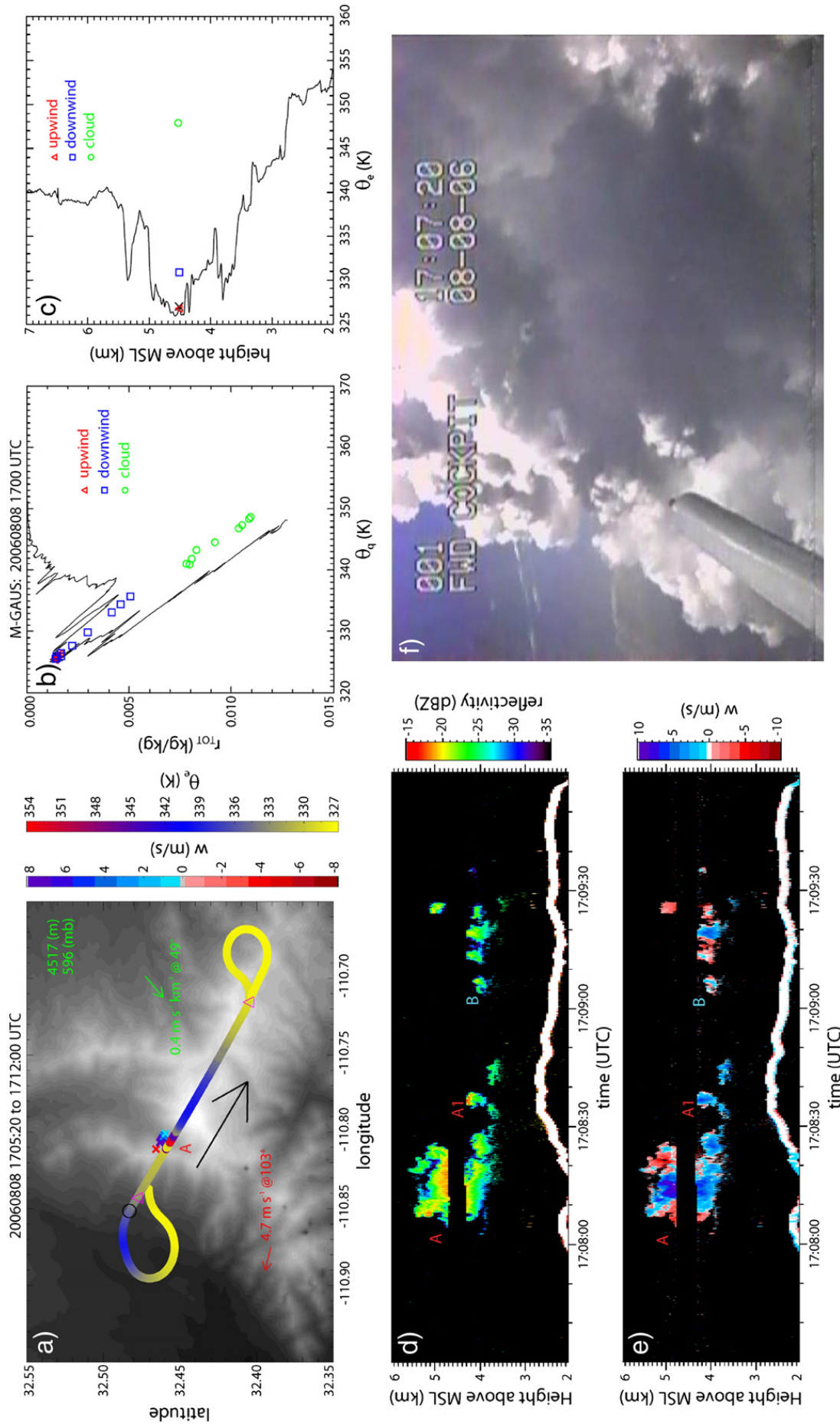


Fig. 9. As Fig. 8, but for the WKA flight track from 1705:20 to 1712:00 UTC.

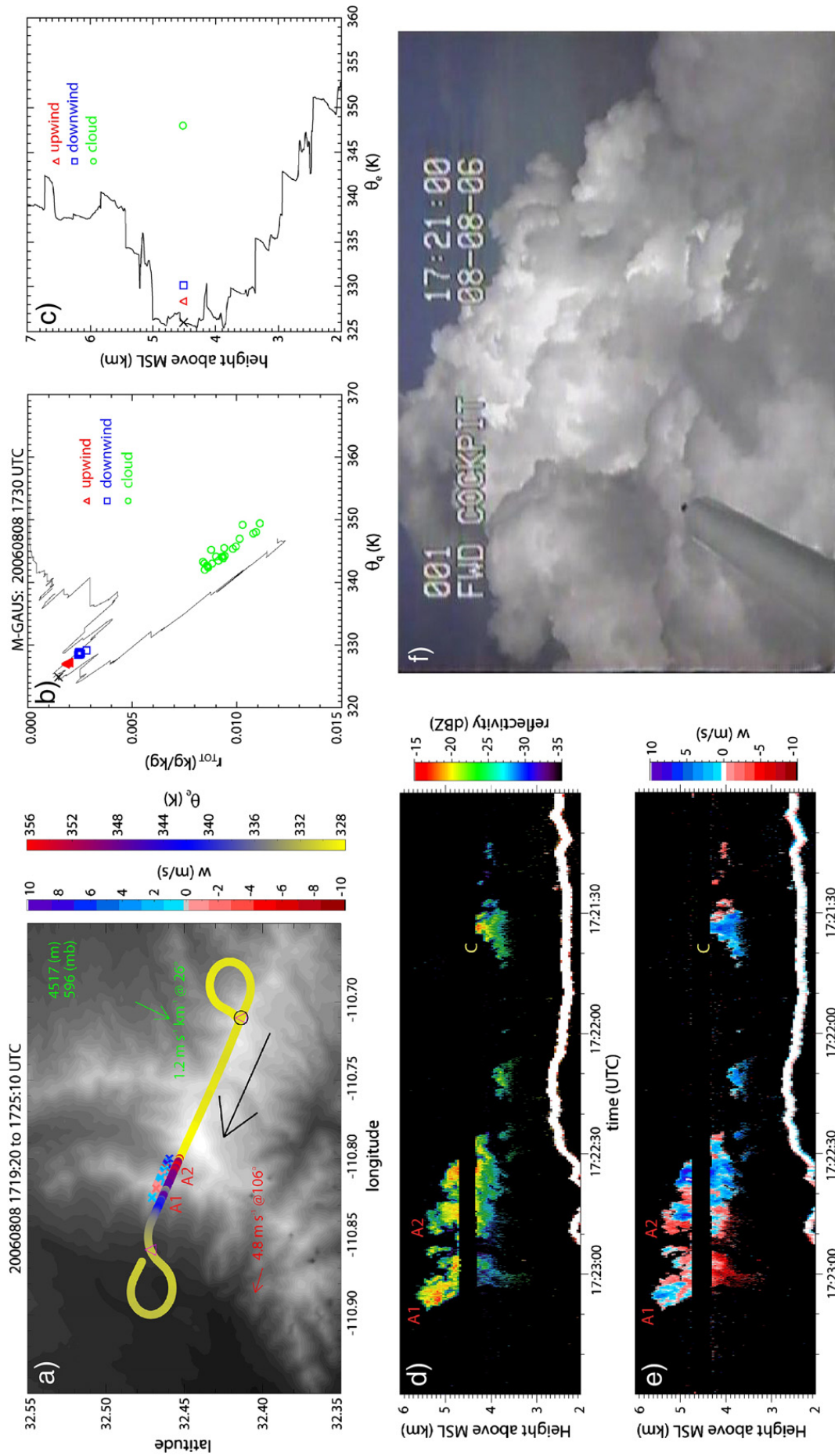


Fig. 10. As Fig. 8, but for the WKA flight track from 1719:20 to 1725:10 UTC.

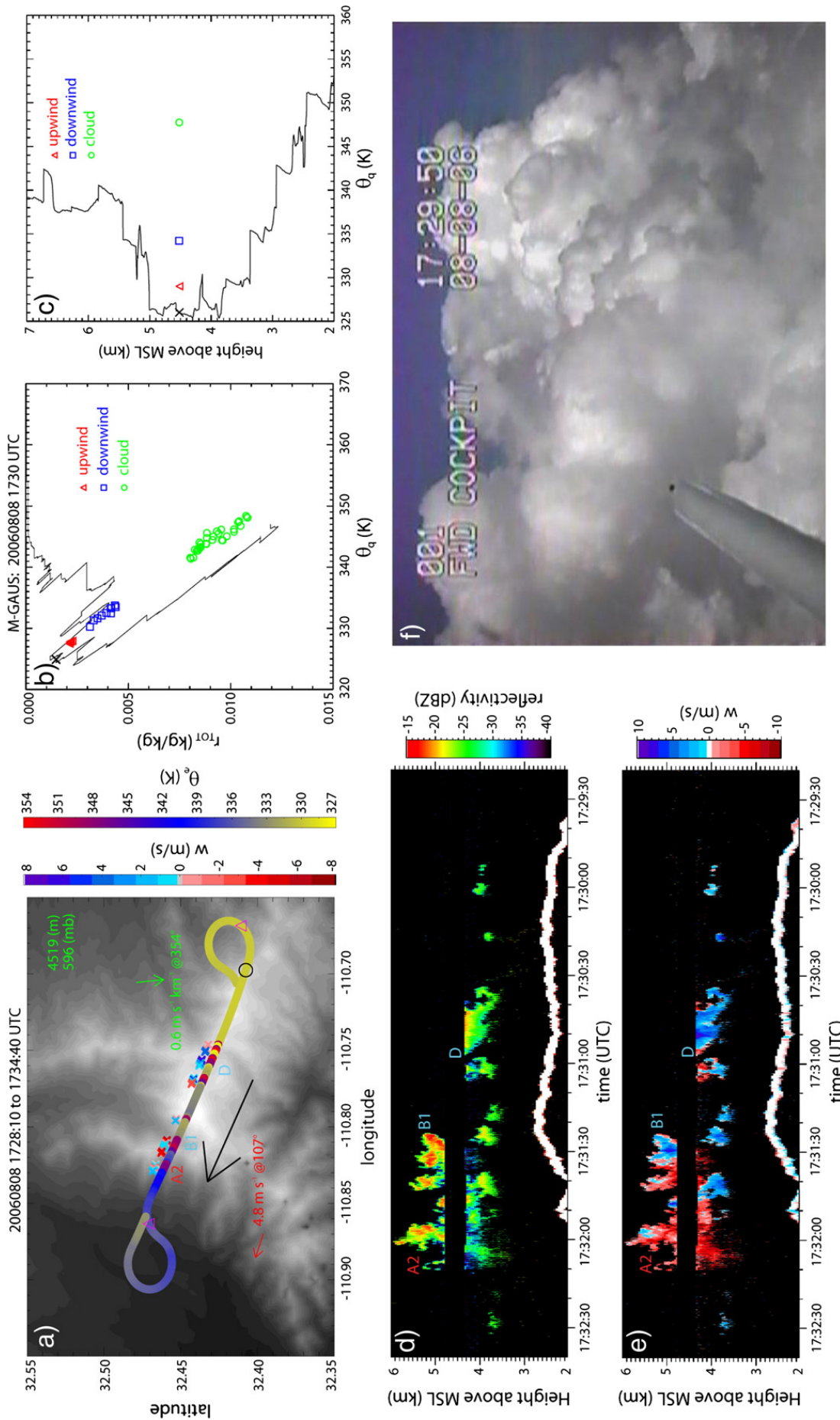


Fig. 11. As Fig. 8, but for the WKA flight track from 1728:10 to 1734:40 UTC.

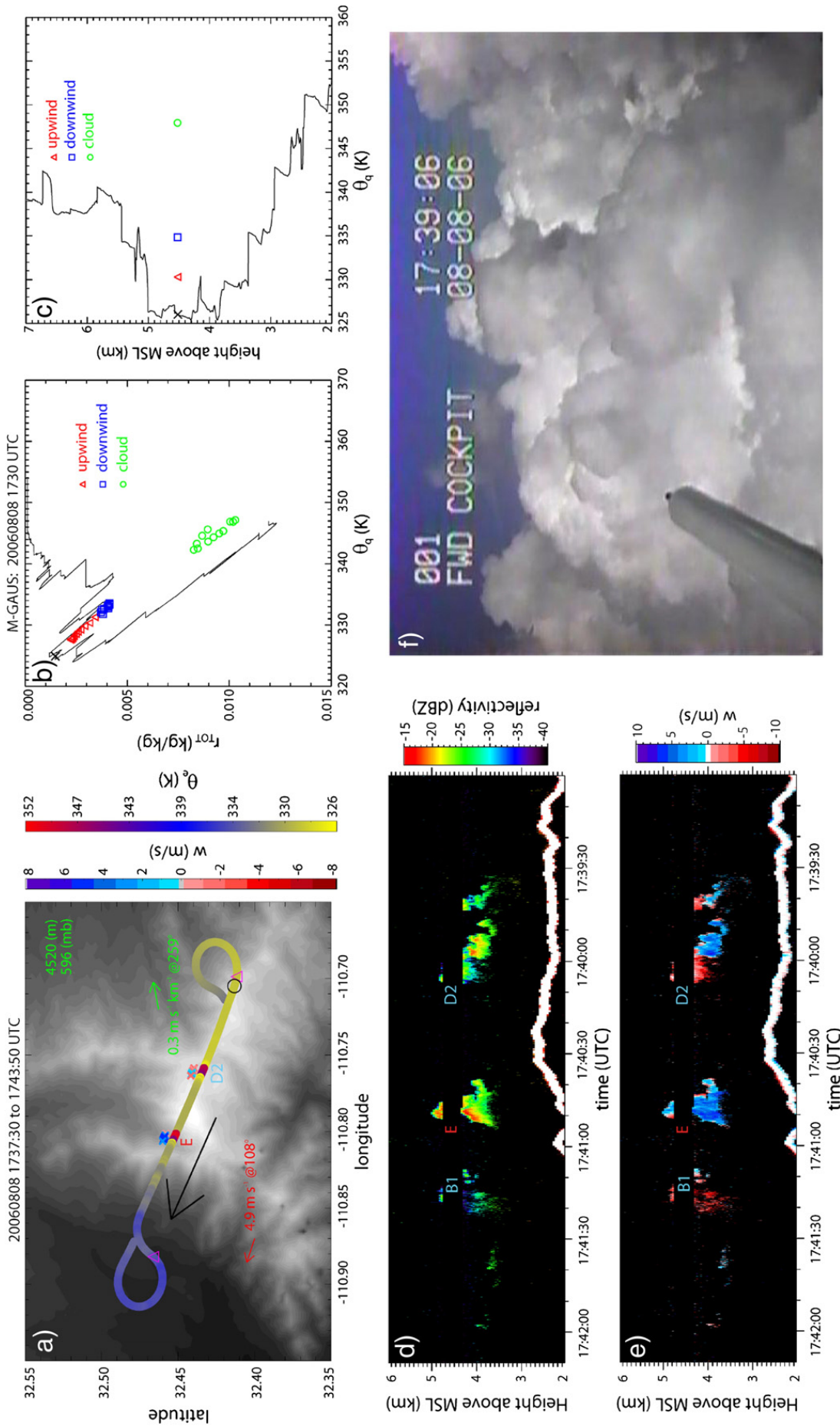


Fig. 12. As Fig. 8, but for the WKA flight track from 1737:30 to 1743:50 UTC.

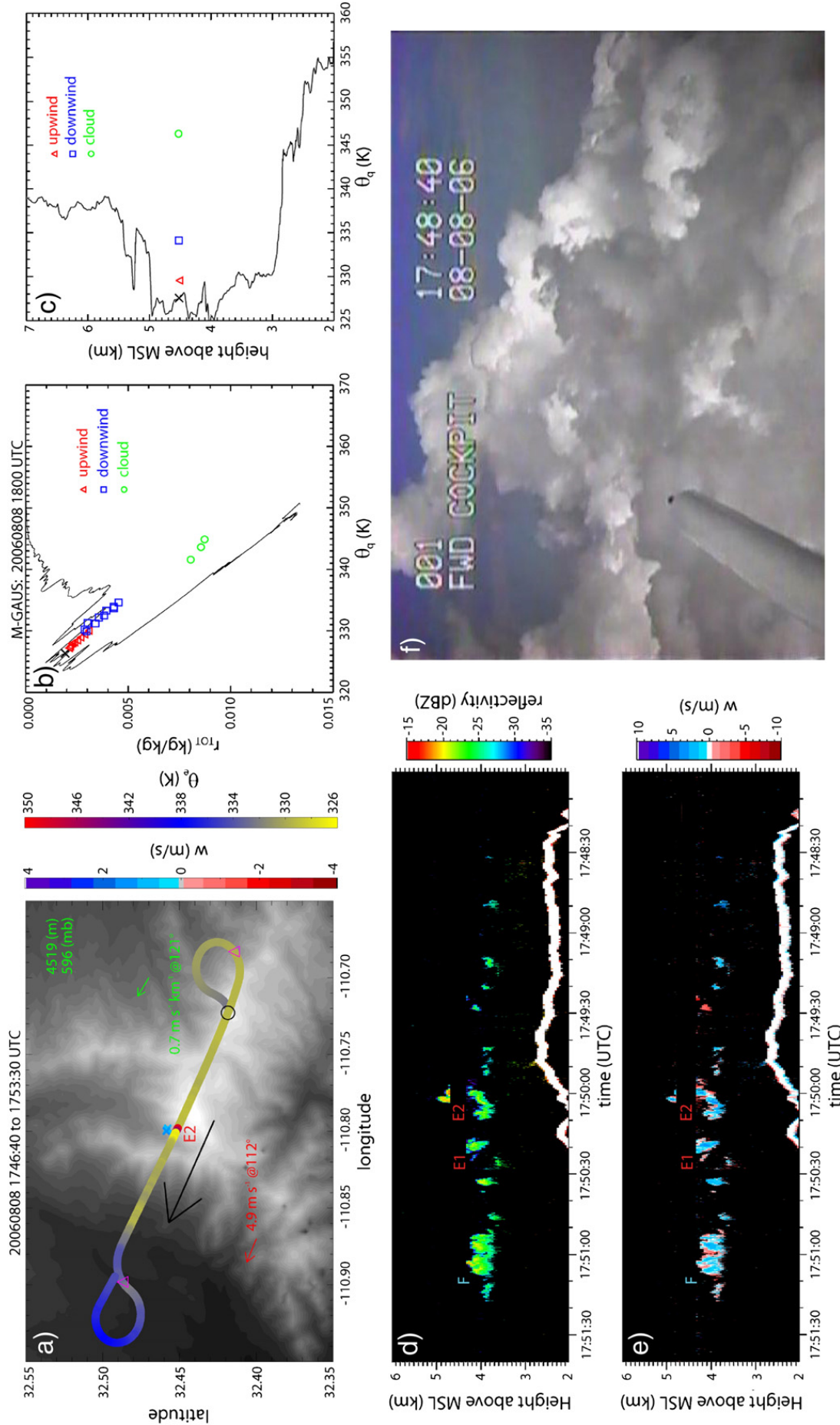


Fig. 13. As Fig. 8, but for the WKA flight track from 1746:40 to 1753:30 UTC.

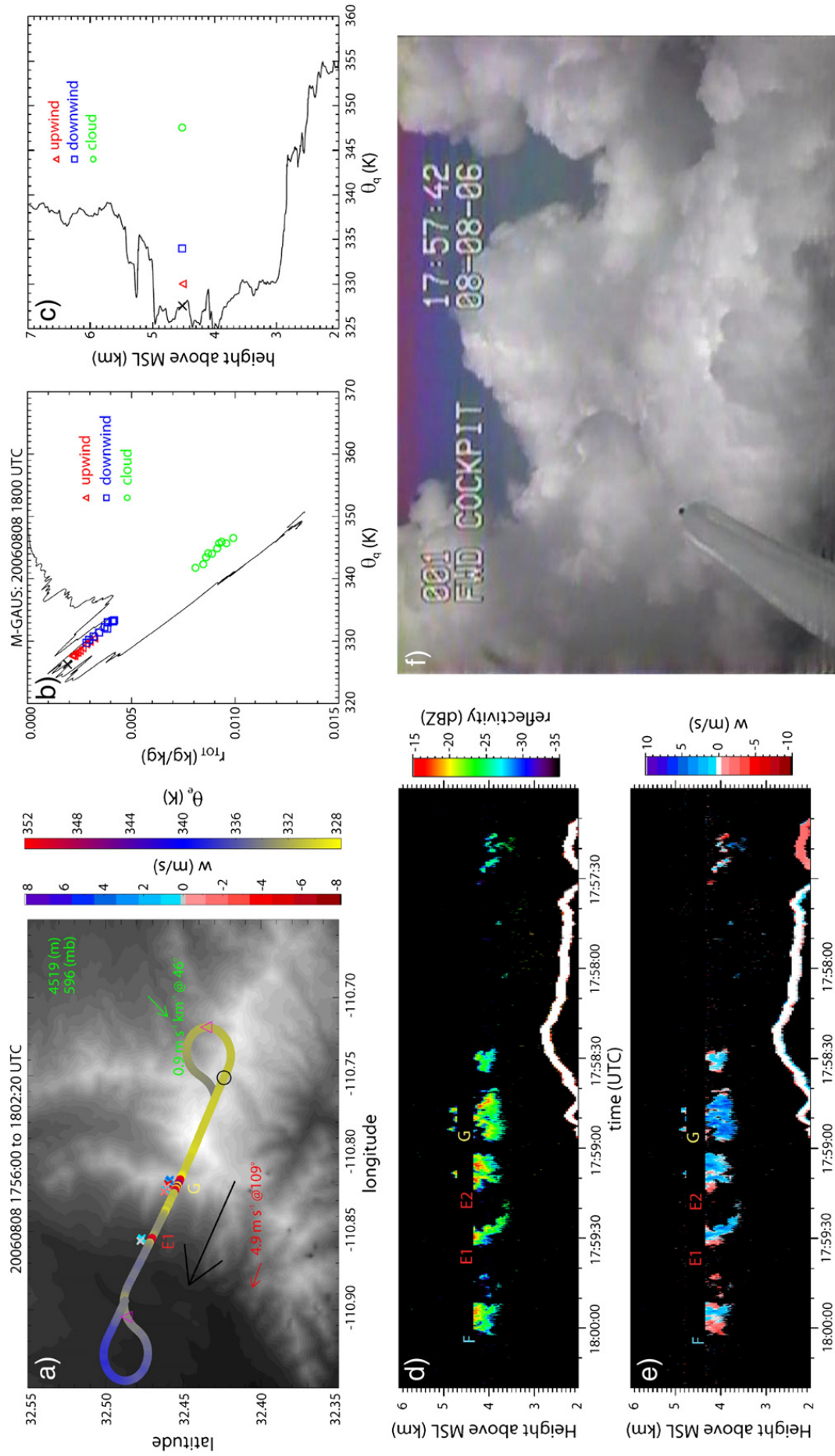


Fig. 14. As Fig. 8, but for the WKA flight track from 1756:00 to 1802:20 UTC.

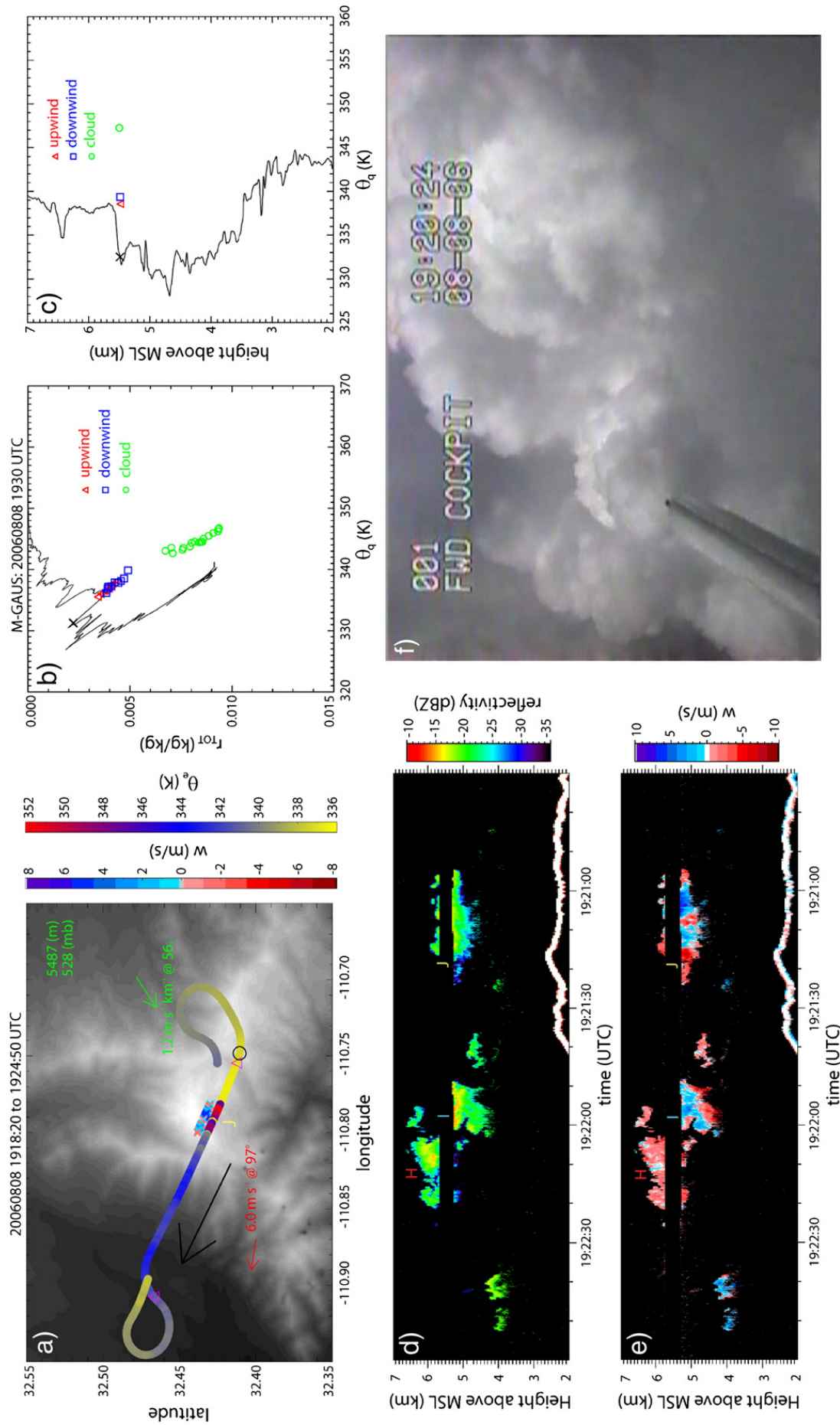


Fig. 15. As Fig. 8, but for the WKA flight track from 1918:20 to 1924:50 UTC.

4. Discussion

4.1. Could the observed differences across the mountain be due to waves in stratified flow?

We have attributed the observed changes in the environment to Cu detrainment and decay, but we have neglected the possibility of stationary gravity waves in stratified flow crossing the mountain. Such waves could explain differences in θ , and thus also in θ_e , between the upwind and downwind loops flown at constant pressure levels. The M-GAUS soundings indicate that the level of minimum θ_e was situated close to the flight level of 4.5 km (panel (c)). This implies that both subsidence and ascent can advect higher θ_e values.

Persistent vertical motion patterns are expected in stationary gravity waves. The average gust probe vertical velocity along all flight loops shown in Fig. 8–Fig. 15 is $-0.27 \pm 0.14 \text{ m s}^{-1}$. This subsidence, both upwind and downwind of the Cu convection, is suggestive of compensating motion. On average this subsidence is slightly (0.08 m s^{-1}) stronger along the loops downwind of the mountain than in the upwind loops. However, the gust probe vertical velocity, based on an inertial navigation system corrected by GPS position measurements, carries an uncertainty larger than 0.08 m s^{-1} (ranging from 0.1 m s^{-1} along straight legs to 0.5 m s^{-1} in steep turns; A. Rodi, pers. comm.). The sequence of soundings may be a better indicator of any persistent vertical motion than gust probe vertical velocity data. The stable layer between 6.5 and 7.0 km MSL (Section 3.3) subsided slowly, according to the series of M-GAUS soundings (Fig. 4). The corresponding mean vertical motion, from the first to the last sounding, is a mere -0.03 m s^{-1} . In short, there is some evidence for widespread subsidence, but no evidence for differential vertical motion between upwind and downwind legs. Specifically at flight level the series of nine M-GAUS soundings do reveal some changes in θ_e (Fig. 5), mainly due to mixing ratio variations, but they were not unidirectional between 1530 and 1930 UTC, and there were no vertically shifting stable layers near flight level.

Neither flight-level vertical velocity differences across the mountain nor the time series of upwind soundings provide adequate evidence for the presence or absence of undulating isentropes. Linear theory predicts that stratified flow over an isolated mountain generates a standing wave pattern with an upwind ridge and downwind trough at low levels, as long as $\frac{N\alpha}{U} \gg 1$, where N is the Brunt–Vaisala frequency, α the half-width of the mountain, and U the mean wind speed (e.g., Durran, 1990). The same basic ridge/trough pattern applies in nonlinear flow regimes (e.g. Section 5.3.1 in Lin, 2007). The M-GAUS data between the surface and 4.5 km MSL yield, on average, $\frac{N\alpha}{U} \cong \frac{0.87 \cdot 10^{-2} \text{ s}^{-1} \cdot 12 \cdot 10^3 \text{ m}}{3.5 \text{ m s}^{-1}} = 30 \gg 1$. An upwind ridge and a downwind trough imply a higher θ and lower r_v in the downwind loops, compared to the upwind loops at the same pressure level, given the mean profiles of θ and r_v (Fig. 5a and c). Instead, a higher r_v is generally observed downwind [panel (b) in Fig. 8–Fig. 15; Fig. 16c], while θ is about the same in upwind and downwind loops, on average, at 4.5 km MSL (Fig. 16a).

Thus the observed difference across the mountain cannot be explained by a stationary gravity wave, and the observed enrichment of θ_e and r_v as the flow passes across the mountain hot spot must be due to the detrainment/decay of orographic

Cu clouds. The downwind–upwind differences in θ_e (Fig. 16b) can be largely attributed to differences in moisture (Fig. 16c), not differences in θ (Fig. 16a). The latter are much smaller than $\Delta\theta_e$, and they are difficult to interpret, as they are affected by several processes, including Cu detrainment/decay, latent heating, ambient vertical motion over the terrain or in response to convection, and solenoidal forcing.

4.2. Moisture-convection feedback

The hypothesis of moisture-convection feedback (or convective conditioning) states that the immediate environment of Cu clouds is modified by preceding convective towers such that Cu growth is facilitated, most likely by the moistening of the environment, which weakens the erosive effect of entrainment. This hypothesis was first examined in early numerical studies of entrainment and in laboratory experiments (Scorer, 1957; Squires and Turner, 1962; Warner, 1970; Cotton, 1975), and gained support amongst modelers aiming to capture the large-scale spatio-temporal characteristics of tropical oceanic deep convection (e.g., Randall and Huffman, 1980; Grabowski and Moncrieff, 2004; Derbyshire et al., 2004). To the authors' knowledge, this hypothesis has not been experimentally verified at the scale of individual Cu clouds.

There is little doubt that orographic convection enriched the environment with CBL air in the present case study. In 16 of the 18 constant-elevation upwind–downwind loop pairs flown, θ_e was enhanced in the downwind loop (Fig. 16). The θ_e enrichment generally was stronger at mid-levels (flight level 4.5 km MSL) than at higher levels (above 5 km MSL). An increase of θ_e near the level of minimum θ_e clearly decreases the lower-tropospheric potential instability. Potential instability could have been further impeded by a decrease in θ_e in the CBL, as the decaying Cu convection on the west side of the mountain advected lower θ_e values down into the CBL, but there is no evidence for this. No convective downdrafts into the CBL were observed by the WCR however [panel (e) in Fig. 8–Fig. 15]. Clearly the collapsing Cu towers lacked the concentrations of hydrometeors needed to sustain a near-moist-adiabatic lapse rate. Moreover, the downwind ISFF stations do not reveal any surface cooling or moistening that would be associated with convective downbursts.

While potential instability decreased in the Cu cloud layer, the absolute and relative humidity generally increased in the downstream environment (Fig. 16c and d), especially at the lowest flight level, where the upwind environment was relatively dry (Fig. 5c). Clearly no new convection developed downstream of the orographic Cu simply because the air had been advected away from the “hot spot” over elevated terrain. But it is possible, in theory, that the successive deepening of the Cu towers over Mt. Lemmon was affected by moistening of the lower cloud layer by a series of shallow Cu growing upstream, over Bigelow Ridge. This would serve as some confirmation of the moisture-convection feedback hypothesis. The time scale of advection over the hot spot (in particular, the 18 km along-wind distance over Bigelow Ridge towards Mt. Lemmon) is about 60–70 min, which is long compared to the life cycle of Cu *mediocris*. Time lapse photography and WCR sequences (Fig. 6) confirm that some Cu go through an entire lifecycle along Bigelow Ridge before reaching Mt. Lemmon at its western end.

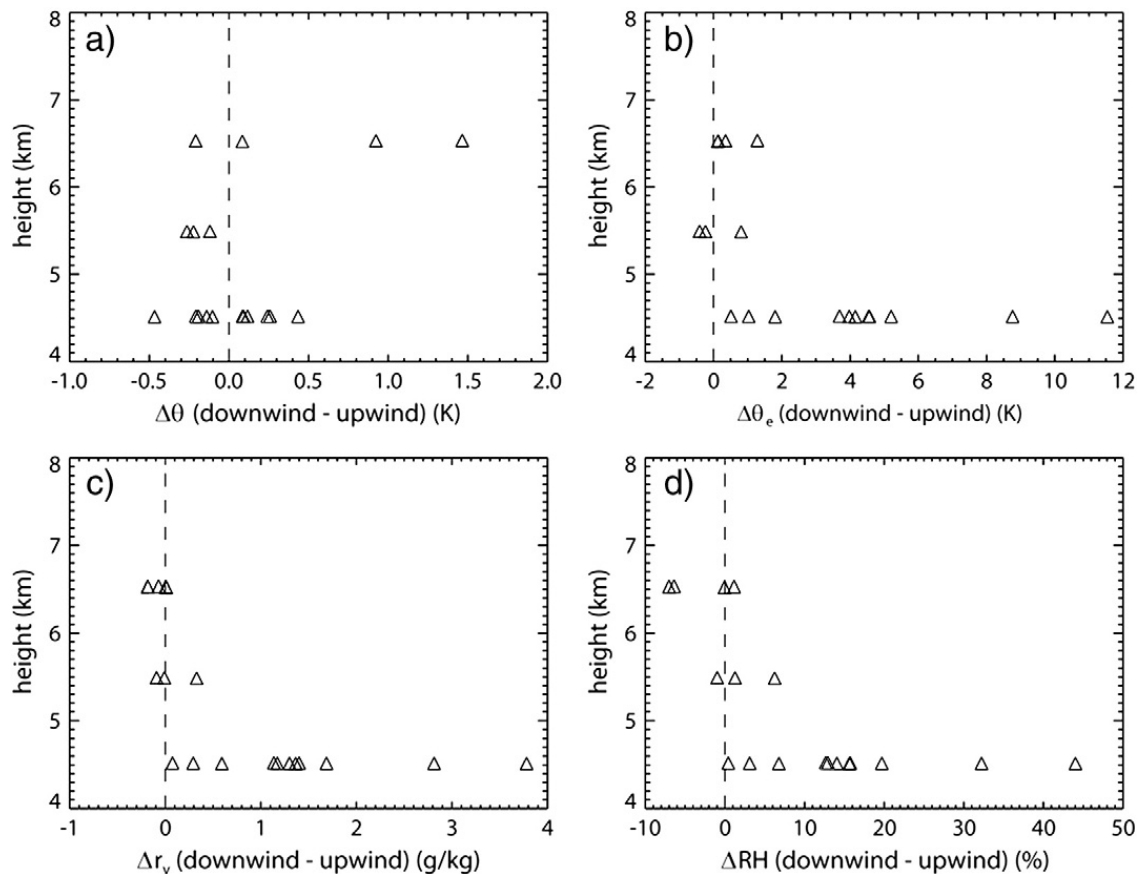


Fig. 16. Scatter plot of the average (a) θ difference, (b) θ_e difference, (c) r_v difference, and (d) relative humidity difference between downwind and upwind loops as a function of flight level, for all downwind–upwind loop pairs flown at constant flight level on 8 August 2006.

Clearly the gradual growth of the orographic Cu complex between 1600 and 1800 UTC (before solar noon) is not a convective conditioning process, but most likely explained simply by steady surface warming (Fig. 3c), leading to an increase in CAPE (Fig. 3b). Still, the continued growth of the Cu towers over Mt. Lemmon in a period of rapid CAPE decline (between 1800 and 1950 UTC Fig. 3a) may have been facilitated by an increase in humidity in the shallow Cu layer over Bigelow Ridge. In conclusion, while it is possible that successive Cu towers over Mt. Lemmon grew more readily in the humid debris of decaying Cu clouds, the hypothesis that convective conditioning explains the commonly observed gradual deepening of daytime orographic Cu over meso- γ scale mountains such as the Santa Catalina Mountains [proposed by Zehnder et al. (2009)] is unlikely to be valid: the convective debris is readily blown off, and the gradual growth is more readily explained by changes in CAPE over elevated terrain.

4.3. Downstream enrichment level

We now examine the vertical distribution of enrichment of the Cu layer with CBL air. It is customary to estimate the detrainment level from sounding data, e.g. by calculating the vertical profile of a variable z^* (Taylor and Baker, 1991):

$$z^*(p) = \frac{\Delta\theta_v(F=1)}{\left. \frac{d\theta_v}{dz} \right|_{ma} - \left. \frac{d\theta_v}{dz} \right|_{env}} \quad (1)$$

where θ_v is the virtual potential temperature, F is the fraction of undiluted cloudy air, and ma and env represent the cloudy parcel following a moist adiabat and of the environment respectively. Detrainment occurs when parcel buoyancy decreases with height, since the lower region of a buoyant cloud parcel then is accelerated faster than its upper region. Thus, detrainment is expected to occur mainly in a region where z^* is negative. Since buoyancy is proportional to the difference of virtual potential temperature between the cloudy parcel and environmental parcel, $|z^*|$ (where $z^* < 0$) represents a vertical length scale over which a cloudy parcel loses its buoyancy. The shorter this length scale (or the larger $|1/z^*|$), the more pronounced the detrainment level. Setting $F=1$ implies an undiluted parcel and thus represents an upper limit. Profiles of $1/z^*$ are estimated from the two representative M-GAUS soundings (Fig. 17a). Both soundings reveal a significantly negative value of $1/z^*$ in the layer between 6.1 and 6.6 km MSL. This is consistent with the potential temperature profile (Fig. 4d–e): a stable layer was present near 6.5 km MSL. The WKA did fly at this level at a later time, between 1930 and 2020 UTC, when the stable layer had weakened (Fig. 4). The four upwind–downwind pairs collected at 6.5 km did not yield a stronger detrainment signature (Fig. 16b): the θ_e difference was smaller than for the pairs of data collected at 4.5 km. The relative humidity in the upwind loops actually was slightly higher than in the downwind loops at the 6.5 km flight level (Fig. 16d), but in fact the upwind air was close to saturation at this level (Section 3.3; Fig. 5c).

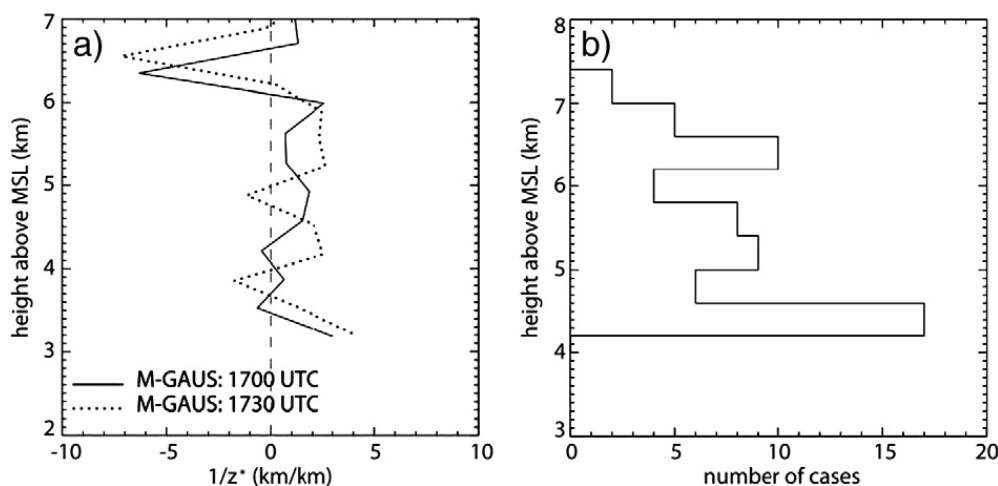


Fig. 17. (a) Vertical distribution of the detrainment parameter $1/z^*$ for M-GAUS soundings launched at 1700 and 1730 UTC. (b) Distribution of Cu cloud top heights over the Santa Catalina Mountains between 1657 and 2013 UTC, based on WCR profiles.

This detrainment level (6.1–6.6 km) represents an upper limit because it assumes no entrainment. Flight-level data can be used to estimate the vertical distribution of downwind enrichment, but there were only three flight levels, with the majority of the flight legs at 4.5 km. Typically most detrainment occurs near the top of Cu clouds (e.g., de Rooy and Siebesma, 2010). The highest cloud top in the orographic Cu complex (Fig. 3a) does not reveal the presence of a range of tops of individual towers (Fig. 17b). Presumably the vertical distribution of detrainment assumes a similar distribution. Of the eight flight sections shown, the flight level was closer to the tops of Cu in the 5th through the 7th section (Fig. 12–Fig. 14), when Cu convection appeared somewhat suppressed. The detrainment/decay signature [i.e., the difference between upwind and downwind loop (θ_q , r_{TOT})] is not significantly different for these sections, compared to the earlier ones. This suggests that the enrichment by detrainment/decay occurred throughout the Cu layer rather than at any specific level. The enrichment signature is most evident at low levels however, as mentioned before (Fig. 16). We see three non-exclusive reasons for this: firstly, most orographic Cu peaked between 4 and 5 km MSL (Fig. 17b) and thus decayed/detrained at rather low levels. Secondly, the ambient (upwind) θ_e reached a minimum near 4.5 km MSL (Fig. 4), so the detrainment/decay signature was strongest there. And thirdly, the average θ_e in a Cu cloud tends to decrease due to the dry air entrainment into clouds, and thus the air detrained at higher levels is relatively depleted of CBL θ_e .

5. Conclusions

In this study mainly three data sources, i.e. in situ, profiling cloud radar and radiosondes, collected as part of the CuPIDO-06 campaign over the Santa Catalina Mountains in Arizona, are combined to study the effect of non-precipitating orographic Cu convection on the ambient air. The main conclusions are as follows.

- The environment downwind of Cu clouds erupting over a hot spot, such as a mountain, is clearly enriched with boundary-layer air. This enrichment is patchy, rather than continuously decaying with distance from the cloud edge, thus it is mainly

the debris of individual Cu towers rather than detrainment from long-lived convection. The enrichment in θ_e across the mountain is not an artifact of stratified flow over the mountain, as it is due not to an increase in θ , but rather an increase in humidity.

- The fraction of air originating from Cu clouds in air parcels downwind of the mountain can be estimated from a Paluch diagram showing the cloudy air, the upwind air, and the downwind air, all at the same level. Some air parcels, sampled 5–20 km downwind of the clouds, still mostly contain orographic cloud residue.
- A downwind enrichment signature is apparent across the entire orographic Cu layer, rather than just a specific level.
- This enrichment in θ_e reduces potential instability in the lower troposphere but convection also increases ambient humidity, thus it may render the downwind environment more conducive to penetrative convection, as entrainment becomes less erosive. This mechanism (known as the moisture-convection feedback mechanism) may affect orographic convection, but it is unlikely to explain the commonly observed gradual deepening of daytime convection over meso- γ scale (~ 20 km) mountains, since the mid-tropospheric plume of modified air usually is blown off the mountain before new convection can bubble up.

These conclusions may be rather intuitive, but the fine detail of this analysis, enabled by high-resolution airborne cloud radar data and numerous soundings in close proximity, is unprecedented. Clearly the conclusions are preliminary, because they are based on a single case study, and they should be validated through other case studies and numerical simulations.

Acknowledgements

This work was supported by National Science Foundation (NSF) grants ATM-0444254 and ATM-0849225. We thank the crew of the University of Wyoming King Air for collecting the data and providing high-quality products for the CuPIDO-06 campaign. This paper benefitted from discussions with Wojciech Grabowski and Jeffrey French. The cloud top chronology was provided by Joseph A. Zehnder.

References

- Barnes, G.M., Fankhauser, J.C., Browning, W.D., 1996. Evolution of the vertical mass flux and diagnosed net lateral mixing in isolated convective clouds. *Mon. Wea. Rev.* 124, 2764–2784.
- Blyth, A.M., 1993. Entrainment in cumulus clouds. *J. Appl. Meteor.* 32, 626–641.
- Blyth, A.M., Cooper, W.A., Jensen, J.B., 1988. A study of the source of entrained air in Montana cumuli. *J. Atmos. Sci.* 45, 3944–3964.
- Bolton, D., 1980. The computation of equivalent potential temperature. *Mon. Wea. Rev.* 108, 1046–1053.
- Brenguier, J., Baumgardner, D., Baker, B., 1994. A review and discussion of processing algorithms for FSSP concentration measurements. *J. Atmos. Ocean. Tech.* 11, 1409–1414.
- Bretherton, C.S., Smolarkiewicz, P.K., 1989. Gravity waves, compensating subsidence and detrainment around cumulus clouds. *J. Atmos. Sci.* 46, 740–759.
- Carpenter, R.L., Droegemeier, K.K., Blyth, A.M., 1998a. Entrainment and detrainment in numerically simulated cumulus congestus clouds. Part II: cloud budgets. *J. Atmos. Sci.* 55, 3433–3439.
- Carpenter, R.L., Droegemeier, K.K., Blyth, A.M., 1998b. Entrainment and detrainment in numerically simulated cumulus congestus clouds. Part III: parcel analysis. *J. Atmos. Sci.* 55, 3440–3455.
- Cho, H., 1985. Rates of entrainment and detrainment of momentum of cumulus clouds. *Mon. Wea. Rev.* 113, 1920–1932.
- Cotton, W.R., 1975. Theoretical cumulus dynamics. *Rev. Geophys. Space Sci.* 13, 419–448.
- Damiani, R., Haimov, S., 2006. A high-resolution dual-Doppler technique for fixed multi-antenna airborne radar. *IEEE Trans. Geosci. Remote Sens.* 42, 3475–3489.
- Damiani, R., Vali, G., Haimov, S., 2006. The structure of thermals in cumulus from airborne dual-Doppler radar observations. *J. Atmos. Sci.* 63, 1432–1450.
- Damiani, R., Zehnder, J., Geerts, B., Demko, J., Haimov, S., Petti, J., Poulos, G.S., Razdan, A., Hu, J., Leuthold, M., French, J., 2008. Cumulus Photogrammetric, In-situ and Doppler Observations: the CuPIDO 2006 experiment. *Bull. Amer. Meteor. Soc.* 89, 57–73.
- Demko, J.C., Geerts, B., Zehnder, J., Miao, Q., 2009. Boundary-layer energy transport and cumulus development over a heated mountain: an observational study. *Mon. Wea. Rev.* 137, 447–468.
- Demko, J.C., Geerts, B., 2010a. A numerical study of the evolving convective boundary layer and orographic circulation around the Santa Catalina Mountains in Arizona. Part I: circulation without deep convection. *Mon. Wea. Rev.* 138, 1902–1922.
- Demko, J.C., Geerts, B., 2010b. A numerical study of the evolving convective boundary layer and orographic circulation around the Santa Catalina Mountains in Arizona. Part II: interaction with deep convection. *Mon. Wea. Rev.* 138, 3603–3622.
- Derbyshire, S.H., Beau, I., Bechtold, P., Grandpeix, J.-Y., Piriou, J.-M., Redelsperger, J.-L., 2004. Sensitivity of moist convection to environmental humidity. *Quart. J. Roy. Meteor. Soc.* 130, 3055–3079.
- de Rooy, W.C., Siebesma, A.P., 2008. A simple parameterization for detrainment in shallow cumulus. *Mon. Wea. Rev.* 136, 560–576.
- de Rooy, W.C., Siebesma, A.P., 2010. Analytical expressions for entrainment and detrainment in cumulus convection. *Quart. J. Roy. Meteor.* 136, 1216–1227, doi 10.1002/qj.640.
- Durran, D.R., 1990. Mountain waves and downslope winds. *Atmospheric processes over complex topography*. In: Blumen, W. (Ed.), *Meteorological Monographs*, 23, pp. 59–81.
- Geerts, B., Dejene, T., 2005. Regional and diurnal variability of the vertical structure of precipitation systems in Africa based on spaceborne radar data. *J. Climate* 18, 893–916.
- Geerts, B., Miao, Q., 2005. The use of millimeter Doppler radar echoes to estimate vertical air velocities in the fair-weather convective boundary layer. *J. Atmos. Oceanic Technol.* 22, 225–246.
- Gerber, H., Arends, B.G., Ackerman, A.S., 1994. New microphysics sensor for aircraft use. *Atmos. Res.* 31, 235–252.
- Grabowski, W.W., Moncrieff, M.W., 2004. Moisture-convection feedback in the tropics. *Quart. J. Roy. Meteor. Soc.* 130, 3081–3104.
- Heus, T., van Dijk, G., Jonker, H.J.J., Van den Akker, H.E.A., 2008. Mixing in shallow cumulus clouds studied by Lagrangian particle tracking. *J. Atmos. Sci.* 65, 2581–2597.
- King, W.D., Maher, C.T., Hepburn, G.A., 1981. Further performance tests on the CSIRO liquid water probe. *J. Appl. Meteor.* 20, 195–202.
- Lenschow, D., Miller, E., Friesen, R., 1991. A three-aircraft intercomparison of two types of air motion measurement systems. *J. Atmos. Ocean. Tech.* 8, 41–50.
- Lin, Y.-L., 2007. *Mesoscale Dynamics*. Cambridge University Press. 630 pp.
- Luo, Y., Krueger, S.K., Xu, K., 2006. Cloud properties simulated by a single-column model. Part II: evaluation of cumulus detrainment and ice-phase microphysics using a cloud-resolving model. *J. Atmos. Sci.* 63, 2831–2847.
- Markowski, P., Richardson, Y., 2010. *Mesoscale Meteorology in Midlatitudes*. Wiley-Blackwell. 430 pp.
- Paluch, I.R., 1979. The entrainment mechanism in Colorado cumuli. *J. Atmos. Sci.* 36, 2467–2478.
- Perry, K.D., Hobbs, P.V., 1996. Influence of isolated cumulus clouds on the humidity of their surroundings. *J. Atmos. Sci.* 53, 159–174.
- Raga, G.B., Jensen, J.B., Baker, M.B., 1990. Characteristics of cumulus band clouds off the coast of Hawaii. *J. Atmos. Sci.* 47, 338–356.
- Randall, D.A., Huffman, G.J., 1980. A stochastic model of cumulus clumping. *J. Atmos. Sci.* 37, 2068–2078.
- Randall, D.A., Huffman, G.J., 1982. Entrainment and detrainment in a simple cumulus cloud model. *J. Atmos. Sci.* 41, 2793–2806.
- Scorer, R.S., 1957. Experiments on convection of isolated masses of buoyant fluid. *J. Fluid. Mech.* 2, 583–594.
- Siebesma, A.P., Holtslag, A.A.M., 1996. Model impacts of entrainment and detrainment rates in shallow cumulus convection. *J. Atmos. Sci.* 53, 2354–2364.
- Small, J.D., Chuang, P.Y., 2008. New observations of precipitation initiation in warm cumulus clouds. *J. Atmos. Sci.* 65, 2972–2982.
- Squires, P., Turner, J.S., 1962. An entraining jet model for cumulonimbus updraughts. *Tellus* 14, 3422–3434.
- Stull, R.B., 1988. *An Introduction to Boundary Layer Meteorology*. Kluwer Academic Publishers. 666 pp.
- Taylor, G.R., Baker, M.B., 1991. Entrainment and detrainment in cumulus clouds. *J. Atmos. Sci.* 48, 112–121.
- Wang, Y., Geerts, B., 2009. Estimating the evaporative cooling bias of an airborne reverse flow thermometer. *J. Atmos. Ocean. Tech.* 26, 3–21.
- Wang, Y., Geerts, B., 2010. Humidity variations across the edge of trade wind cumuli: observations and dynamical implications. *Atmos. Res.* 97, 144–156, doi 10.1016/j.atmosres.2010.03.017.
- Warner, J., 1970. On steady-state one-dimensional models of cumulus convection. *J. Atmos. Sci.* 27, 1035–1040.
- Zehnder, J.A., Hu, J., Razdan, A., 2007. A stereo photogrammetric technique applied to orographic convection. *Mon. Wea. Rev.* 135, 2265–2277.
- Zehnder, J.A., Hu, J., Razdan, A., 2009. Evolution of the vertical thermodynamic profile during the transition from shallow to deep convection during CuPIDO 2006*. *Mon. Wea. Rev.* 137, 937–953.